Shi-lin Zhang · Yue-ping Yin · Xie-wen Hu · Wen-pei Wang · Zong-liang Li ·
Xin-ming Wu · Gang Luo · Sai-nan Zhu

Geo-structures and deformation-failure characteristics of rockslide areas near the Baige landslide scar in the Jinsha River tectonic suture zone

Abstract After two successive Baige landslides in the Jinsha River tectonic suture zone, a landslide scar with three steep free surfaces has been exposed in the source area, where three concomitant sliding blocks (K1, K2, and K3) have been identified as continuously moving at high rates, suggesting further potential failures within these areas. This study focused on structural geology and conducted a comprehensive multidisciplinary analysis to understand the active features and geological evolution models for these sliding blocks. Results showed that the three rockslides can be further subdivided into eleven subdomains. The revealed rock masses are likely to be affected by faults, fracture zones, and folds, and are featured by widely distributed and variable interbedded lithology with heterogeneous qualities combined with fragmentation, brecciation, and mylonitization. The movements are gradually increasing, especially encountering rainfall, and are ascribed to the dramatic unloading resulting from sudden large-scale detachments during the successive landslides and subsequent progressive time-dependent strength degradation of the rock masses. The active features and geological evolution models vary for the different subdomains and are intensely associated with daylighting geo-structures. Serpentinite predominates K1-4 and K1-5, showing brittle fracturing after a certain degree of accumulative deterioration is surpassed, highly weathered carbonaceous slate predominates K2-1 accompanied by "back-pushing" of en masse slide, and better rock mass integrity causes K1-3 to exhibit "fore-pulling" of retrogressive superficial collapse.

Keywords Rockslide · Baige landslide · Field investigation · Displacement measurement · Active features · Geological evolution models

Introduction

On October 10 and November 3, 2018, two large-scale landslides successively occurred in the upper reach of the Jinsha River, located at the border between the Sichuan province and Tibet, China (Fig. 1a). In total, these landslides involved ~ 34×10^6 m^3 of sliding masses that rushed into and blocked the Jinsha River, resulting in the formation of dammed lakes twice (Fan et al. 2019; Zhang et al. 2020a, b). The first-formed dammed lake began draining naturally on October 12, 2018, and finally breached on October 12 accompanying by minor flooding. However, the second-formed dammed lake was drained by an artificial diversion channel. During the breaching process of the second-formed dammed lake, the peak dam breaching flow rate was greater than 30,000 m^3/s, which caused great damage to the downstream bridges, roads, and hydropower stations (Li et al. 2019a, b; Zhang et al. 2019).

Considering that the Baige landslide is one of the most representative landslide disasters in recent decades, several studies have been conducted to investigate this disaster chain, such as the basic characteristics and deformation history (Fan et al. 2019; Xiong et al. 2020), initiation mechanisms (Li et al. 2019a, b; Zhang et al. 2020b; Chen et al. 2021), runout processes (Ouyang et al. 2019; Zhang et al. 2020a), and dam breaching processes (Zhang et al. 2019). However, as an important segment for researching this landslide disaster, clarifying the detail of the geo-structures (such as lithologies, faults, folds, and discontinuities) of the Baige landslide and revealing their impacts on the deformation and displacement accumulation processes of the Baige landslide are less. The landslide area belongs to a high-relief mountainous region with active tectogenesis, and long-term geomorphological evolution under river incision made considerable contributions to the progressive deformation of the Baige landslide (Chen et al. 2021). Zhang et al. (2020b) conducted a series of field studies to attempt to understand the geo-structures of the Baige landslide. On this basis, they stressed that, for the Baige landslide area, easily degraded serpentinite and well-developed foliation were the failure-prone structures, and active tectogenesis was a crucial source to kinematic release. These research findings have laid the foundation for our present study.

After two successive failures on the Baige landslide, a landslide scar with three steep free surfaces has been exposed in the source area due to stress redistribution after dramatic unloading and rebounding, where three concomitant unstable rockslide blocks (K1, K2, and K3) are distributed (Fig. 2) with the volumes of ~ 226.2×10^4 m^3, ~ 595.07×10^4 m^3, and ~ 119.56×10^4 m^3, respectively. As of November 2020, these rockslides have been affected by two rainy seasons. It has been identified that these blocks are continuously moving at high rates, thereby suggesting potential failures within these areas. Some remedial measures, such as unloading, were carried out on the top of rockslides from June to November 2019, to avoid failure again within these rockslide areas. However, for these three rockslide blocks, knowledge of the internal geo-structures, mechanisms that control slope movement, and related geological evolution, which can help identify predictive precursors (Ganerød et al. 2008; Willenberg et al. 2008a, b), is currently unavailable. Therefore, in this study, we conducted a multidisciplinary analysis of the rockslide areas to (i) describe the detailed geology
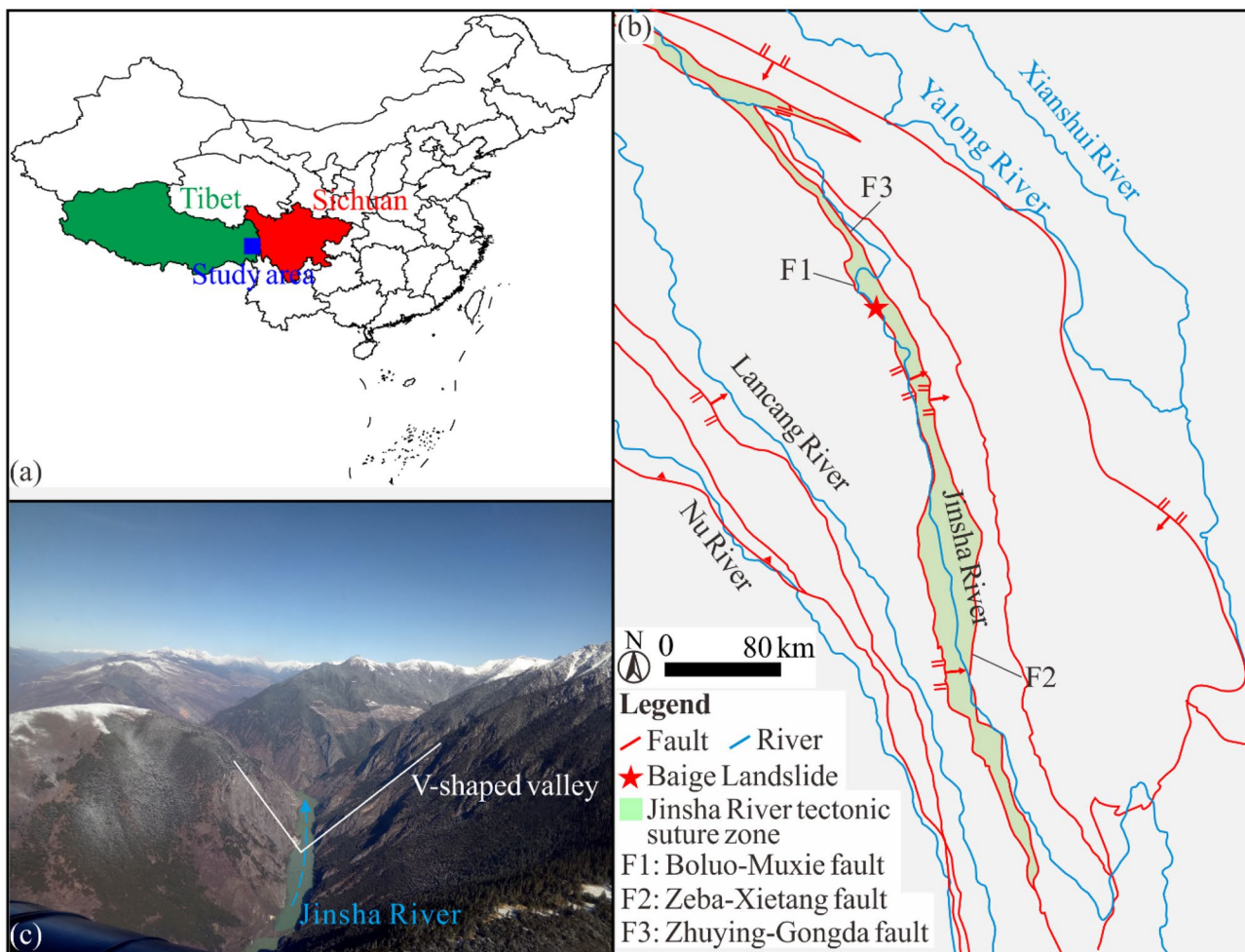
Fig. 1 Location and regional background of the study area: **a** location of the Baige landslide, **b** regional geological background, and **c** regional topographic feature

using comprehensive field investigation, (ii) understand the active features by employing a real-time monitoring network and multiphase field observations, and (iii) propose geological evolution models for further numerical analysis.

Setting

Regional geological background

The Baige landslide developed within the Jinsha River tectonic suture zone (Fig. 1b). This suture zone is considered to be a back-arc basin on the eastern margin of the Paleo-Tethys, which was formed in the Devonian-Carboniferous. In terms of geotectonics, the collision around the Permian–Triassic boundary to the Middle Triassic led to the closure of the back-arc basin and the formation of the suture (Wang et al. 2000). Since the Paleozoic, the Jinsha River tectonic suture zone has experienced opening, spreading, shrinking, and closing. Then, the tectonesis in the Jinsha River tectonic suture has been very intense, resulting in the development of the NS-striking ductile shear zone and the well-developed schistosity zone, and a series of EW-striking compressional imbricate thrust nappe and fold structures (Cao et al. 2015). Due to the characteristics

of polyphase tectogenesis (Fan et al. 2019; Zhang et al. 2020a, b), the tectonic structure in this suture is quite complex, mainly including a larger number of different-scale NW-striking faults. As shown in Fig. 1b, F1, F2, and F3 are regarded as the predominant faults and form the boundary of the Jinsha River tectonic suture.

The rock outcropping in the Baige landslide belongs to the Jinsha River serpentinite mélange belt, which is characterized by an extremely complex spatial distribution of lithologies. Based on previous investigations conducted by SHCEC (2013), the strata exposed in the landslide area include the Late Paleozoic Variscan Jinsha River ultramafic belt and serpentinite (φ_{ω_4}), and the Upper Proterozoic Xiongsong group gneiss formation ($P_t xn^a$).

Geomorphology

Polyphase tectogenesis and intense erosion caused by the downcutting of the Jinsha River resulted in a unique topography of steep terrain with high mountains and deep V-shaped valleys (Fig. 1c). The original terrain of the Baige landslide was very steep, exhibiting a front slope angle and a back slope angle of ~ 65° and ~ 35–55°, respectively (Zhang et al. 2020b). The morphology of the landslide
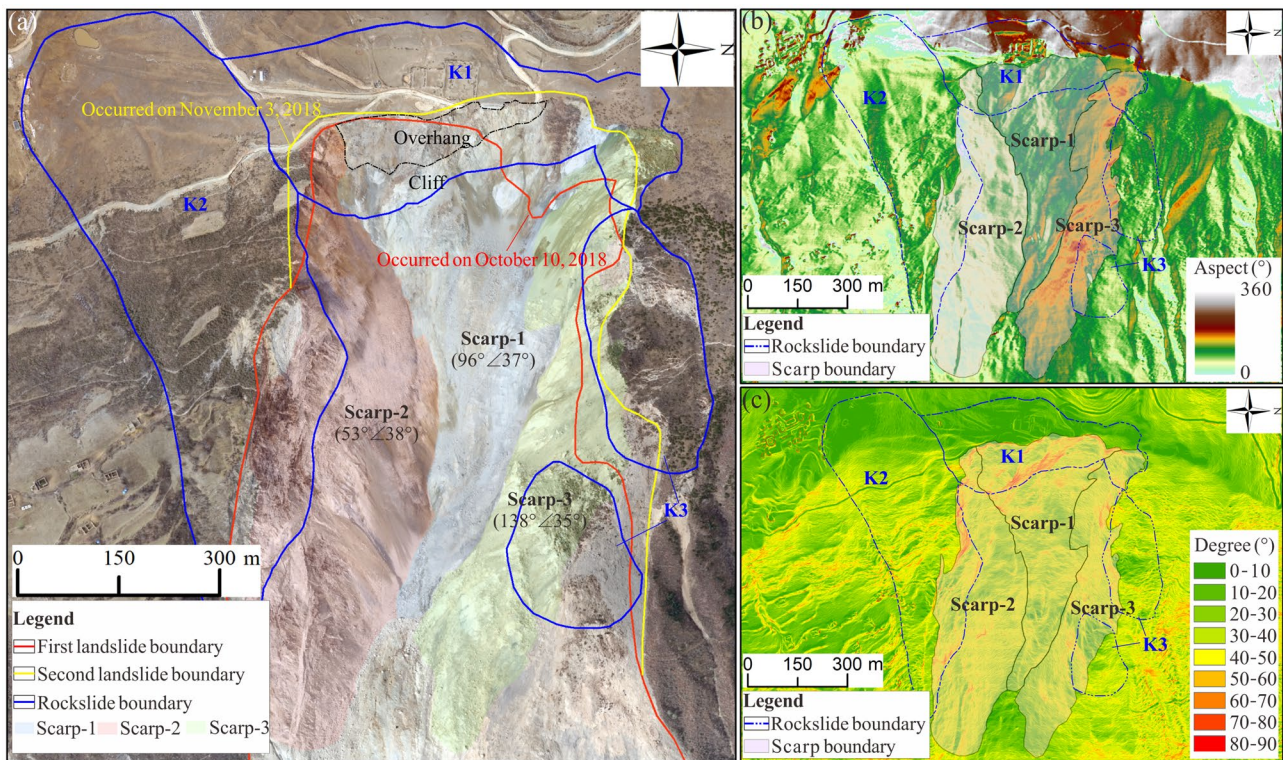
Fig. 2 Geomorphology of the rockslide areas near the Baige landslide scar: **a** three dimensional model of the rockslide areas, **b** slope aspect of the rockslide areas, and **c** slope gradient of the rockslide areas

scar after the successive landslides is shown in Fig. 2. Figure 2 indicates that three huge back scarps are visible (labeled Scarp-1, Scarp-2, and Scarp-3), comprising a total projected area of ~ 0.435 km². Scarp-1 is located on the back side of the landslide scar, with an average orientation of 96°∠37° (dip/dip angle). The terrain of Scarp-1 is observed to be varying. At the upper part of Scarp-1, the terrain is overhanging with a maximum slope gradient of more than ~ 70°. Immediately adjacent, the terrain presents a cliff, on the upper part of which the toe line of K1 is located, with a slope gradient of more than ~ 70°. Toward the lower part of Scarp-1, a gradually narrowing surface inclining from ~ 50° to 0° is visible. Scarp-2 is located on the south side of the landslide scar and expresses an inclined slickenside surface with an average orientation of 53°∠38°. In the upper part of Scarp-2, a dislocated minor scarp with a larger slope gradient of more than 40°, served as the toe of K2, is distributed. Scarp-3 is distributed on the northern side of the landslide scar. Scarp-3 also presents an inclined slickenside surface, with an average orientation of 138°∠35°. At the upper part of Scarp-3, the average slope gradient is approximately 40°, and a series of dislocated minor scarps develop here, which are considered to be the toe line of K3.

Methods

Crack mapping and boundaries of rockslides
After the two successive landslides, a large number of cracks were distributed on the surface of the rockslide areas behind the main

head scarp. The location and orientation of all the cracks were mapped as of October 2019. Additionally, the mechanical and geometrical properties of the deep and large-scale cracks which control the unstable blocks were statistically analyzed. Further, using the structure pattern of these formed cracks and geomorphology of rockslide areas, the boundaries of the rockslide areas were distinguished.

Investigation of geo-structures

Core logging

As shown in Fig. 3, eighteen boreholes were drilled and cored to investigate deep geo-structures. The drilling was divided into two stages, with the first stage being completed in May 2019 (including ZK1–ZK13) and the second in August 2019 (including ZK14–ZK18). All boreholes were vertical, and the depth for each borehole was largely restricted by slurry leakage and hole-wall collapse as a result of fractured rock masses in the study area. The vertical depths of these boreholes were mostly between 50 and 70 m, and the maximum vertical depth was 100 m. All cores were logged, and a rock quality designation (RQD) was obtained. Measurements were taken of the dip direction and dip angle for the metamorphic foliation revealed in the cores. For some representative rock cores, rock-mineral analysis was carried out to determine the mineral composition and distinguish the lithology.
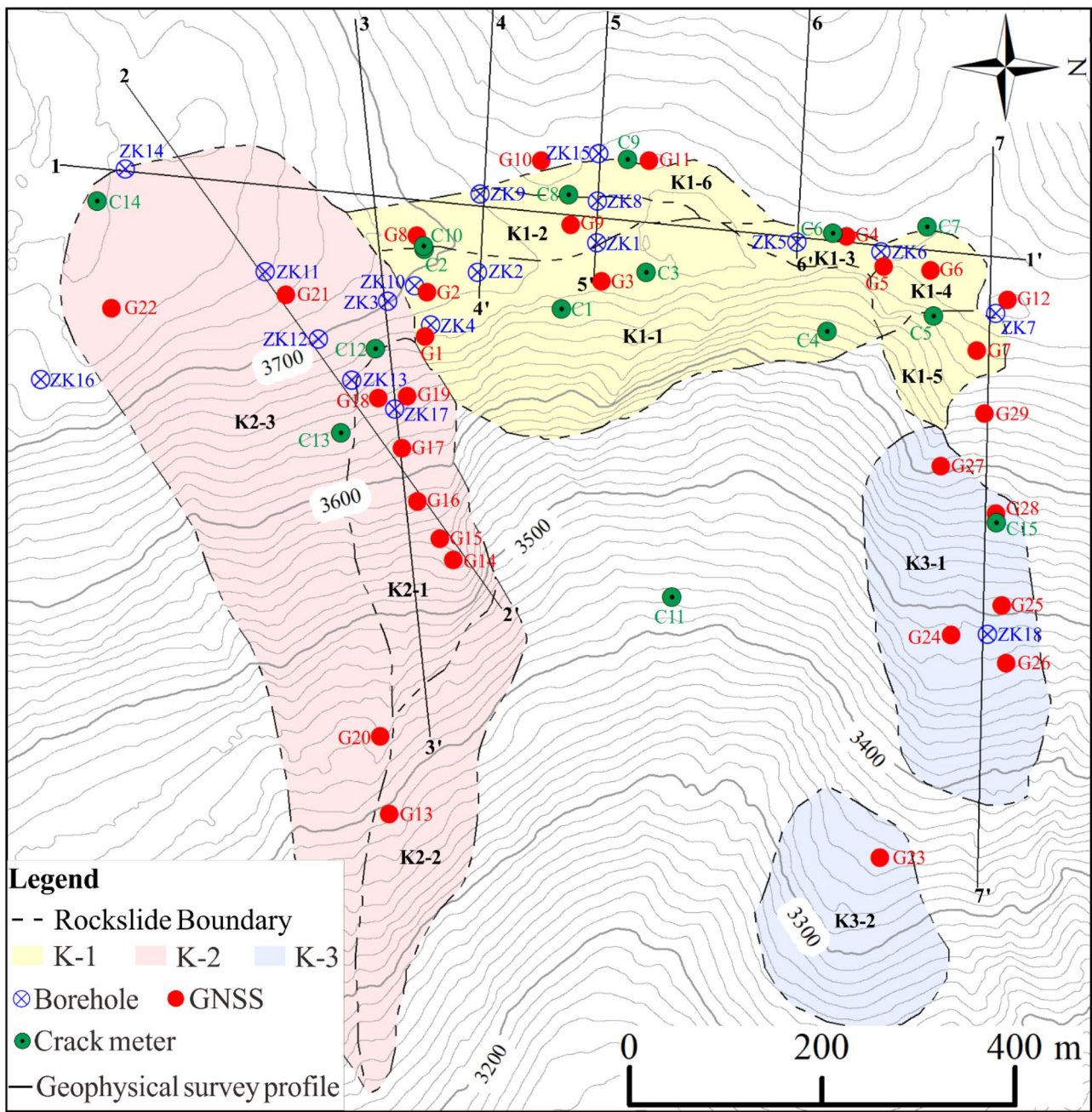
Fig. 3 Layout of the boreholes, GNSS, crack meters, and geophysical survey profiles

Sonic logging of P-wave in borehole

The purpose of sonic logging of boreholes is to determine the propagation velocity of the P-wave in bedrock, which is positively related to the rock mass quality and thereby can be used to discern the relative weakness in bedrock by detecting low or abruptly decreasing P-wave velocity. Here, sonic logging was performed on seven boreholes, including ZK1, ZK3, ZK5, ZK6, ZK9, ZK11, and ZK12. For each borehole, the probe, which consists of one transmitter and two receivers, is able to calculate P-wave velocity automatically at 20 cm intervals.

Surface geophysical mapping

A geophysical survey using an electromagnetic survey was conducted to detect the locations, depth ranges, and orientations of the subsurface geological structures. With respect to different survey depths, audio magnetotelluric sounding (AMS) and multi-electrode resistivity method (MSM) were used, respectively, to map deep structures below ~600 m and ~200 m. The data of both surveys were collected along the same seven profiles (Fig. 3), comprising a total length of ~5359 m. The equipment used in this AMS was a PHOENIX Geophysics System 2000.net model V8. The frequency

of this AMS was from 0.1 Hz to 10 kHz. The processing software SSMT2000 and inversion software MTSoft2D were used for data processing and inversion, respectively. Acquisition of MSM was collected with Wenner, with an electrode spacing of 10 m for profile 1–1′, 2–2′, 3–3′, and 7–7′ and an electrode spacing of 7 m for profile 4–4′, 5–5′, and 6–6′.

Investigation of activity features

Recorded movements of rockslides

To identify the deformation evolution and kinematic characteristics of the unstable areas, a real-time monitoring network consisting of several monitoring instruments was installed on the unstable areas after the first landslide, but many monitoring instruments were removed or destroyed during the unloading process. The measurement of absolute surface displacement was undertaken by Differential Global Navigation Satellite System (GNSS). The measurement principle of GNSS is explained by Böhme et al. (2016). According to GNSS measurements, both the deformation magnitude and vector for monitoring point can be obtained. Additionally, the relative distance measured between two points occurring across surface cracks was measured by crack meters. A total of 29 GNSS instruments and 14 crack meters were installed (Fig. 3). The deadline for all data statistics presented in this study is October 28, 2020.

Multi-phase field observations
Alongside the surface deformation monitoring, multi-phase field observations were simultaneously conducted to observe the activity features of rockslides. In particular, after the completion of unloading on November 2019, the detailed deformation-failure evolution characteristics for these rockslides were visited in the field three times on January 16, 2020, March 12, 2020, and June 1, 2020. During fieldwork observations, newly formed cracks and new deformation-failure phenomenon were recorded.

Results

Crack mapping and boundaries of rockslides
The mapping results of surface cracks at K1, K2, and K3 as of October 2019 are presented in Figs. 4–6, respectively. As shown in Fig. 4, many different-scale arc-shaped cracks are distributed across K1, and almost all of them are tension-induced. Tensional cracks in this area which are sub-parallel to Scarp-1 are very common, striking either approximately NS or EW, which would be favorable for kinematic release toward the free space. Multiple small-scale and dense imbricate cracks are distributed near the free surface, followed by several large-scale transverse cracks showing ongoing extension. The cracks in K2 are shown in Fig. 5. They have disparate strikes corresponding to different mechanical properties, which are the approximately NS-striking tensile cracks, the NW–SE-striking tensile-shear cracks, and the approximately EW-striking shear cracks (Fig. 5a). Several dense arc-shaped NS-striking cracks are well-developed on the middle (Fig. 5b) and north side (Fig. 5c) of K2. For both the lower and upper parts of K2, cracks are relatively scattered without centralized distribution. The distribution characteristics of cracks in K3

are relatively clear, consisting of NS-striking tensile cracks and EW-striking tensional-shear and shear cracks (Fig. 6).

The complex crack frames form the boundaries of the rockslide areas. K1, located behind Scarp-1, resembles an armchair shape and is estimated to be ~ 700 m across-slope and ~ 280 m down-slope. The upper boundary of K1 is marked by the NS-striking transverse tensional crack C11 at ~ 3700 m a.s.l., and the lower toe line is marked by the upper part of the cliff on Scarp-1 at ~ 3480 m a.s.l. (Figs. 2 and 4). K2, located on the southern side of Scarp-2, shows an elongated-strip shape, with an estimated average length and width of ~ 800 and ~ 300 m, respectively. K2 is controlled by the tensional crack C2 and shear crack C21 on the upper boundary, a dislocated minor scarp at the toe, and a narrow gully oriented NE-SW on the southern boundary (Fig. 5). K3, located on the northern side of Scarp-3, is formed by two separate subzones, exhibiting a "tongue" shape in planview. As shown in Fig. 6, the upper boundary, left boundary, and lower boundary are marked by C35 and C33, the shear crack C34, and the dislocated minor scarps on the upper segment of Scarp-3, respectively. Furthermore, based on the differing structure pattern of these formed cracks and the geomorphology of rockslide areas, we further subdivided the three rockslide areas into eleven subdomains (Figs. 3–6), and the boundaries for these subdomains are listed in Table 1.

Investigation of geo-structures

Distribution characteristics of lithology

The cores logged in the boreholes are shown in Fig. 7. Some typical rock exposures observed in the boreholes of the first stage can be found in Zhang et al. (2020b). As shown in Fig. 7, complex lithologic distribution is the primary feature. First, the rocks forming P_txn^a are dramatically diverse, consisting of twenty-one lithologies. In addition to widely distributed gneiss, other lithologies are sporadically exposed. Mylonite, shear zones, and faults are the main contact types between the lithologies. The rocks behind the landslide scar (including K1-1, K1-2, K1-3, and K1-6) are mainly gneiss and schist. On the north side of the landslide scar, K1-4 primarily consists of serpentinite, while the serpentinite in K1-5 presents a concave vein-like distribution, and the front part of K1-5 is especially mingled with relatively intact gneiss (Fig. 8a). However, K3 mainly consists of phyllite without serpentinite, and gneiss is exposed on its lower part (Fig. 8a). Furthermore, in ZK18, we found that the granite porphyry, which is clearly distinguished above the serpentinite on the outcrops of the landslide deposit according to Zhang et al. (2020a), is interbedded with phyllite and is intermittently outcropped with a maximum thickness of ~ 3.5 m (Figs. 7 and 8b). Additionally, the predominate features of the lithologic distribution on the south side include the extensive exposure of carbonaceous rock, as shown in ZK17, where the thickness of such rock is more than 10 m (Fig. 7), and daylighting highly weathered carbonaceous slate is distributed on the lower part of K2-1 (Fig. 8a). In addition, serpentinite exposes ~ 380 m away from Scarp-2 on the right side of the landslide scar according to the logging results of ZK16 (Figs. 7 and 8c), which updates the previous finding that serpentinite is only distributed on the left side of the landslide (Zhang et al. 2020a).
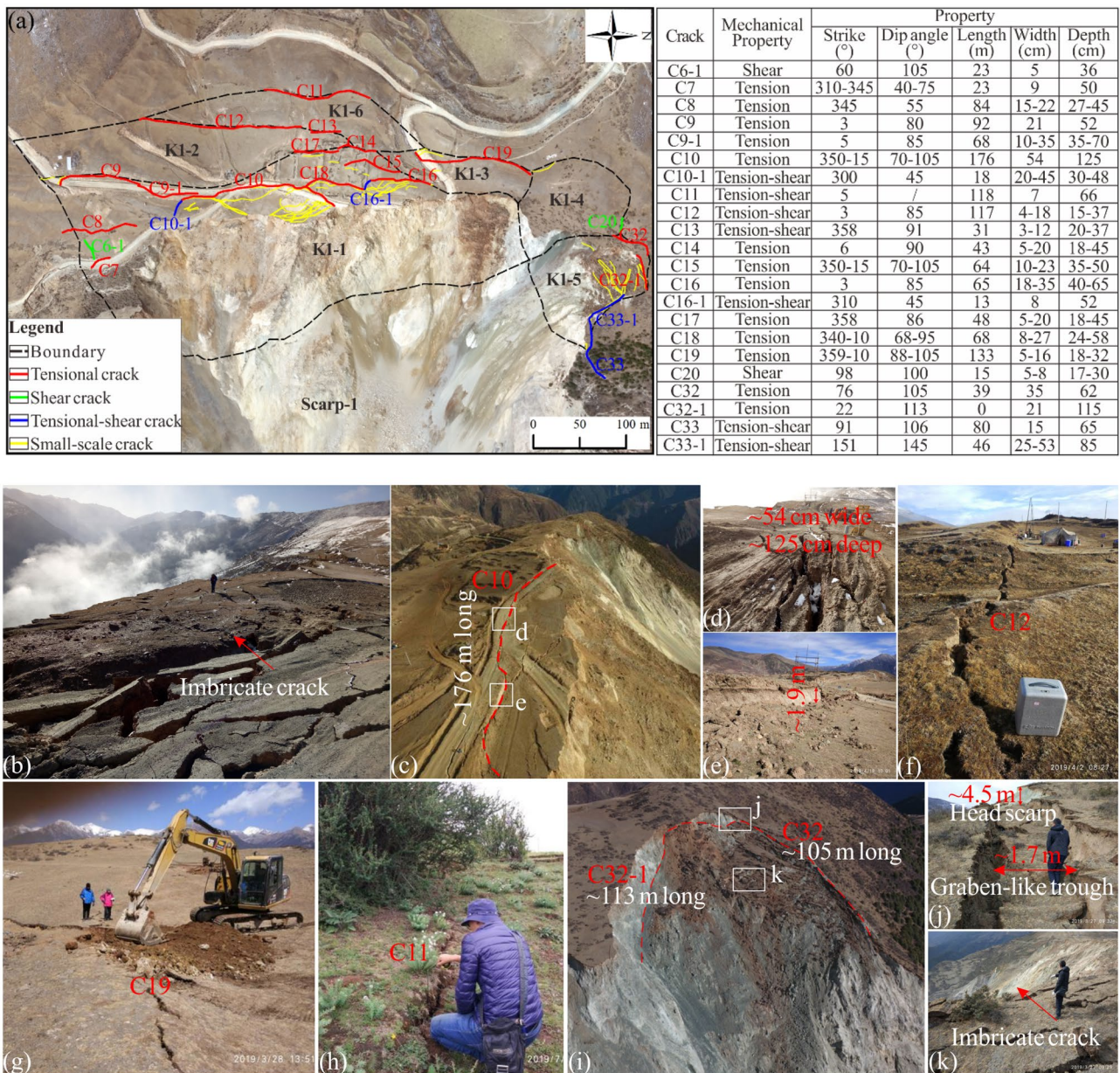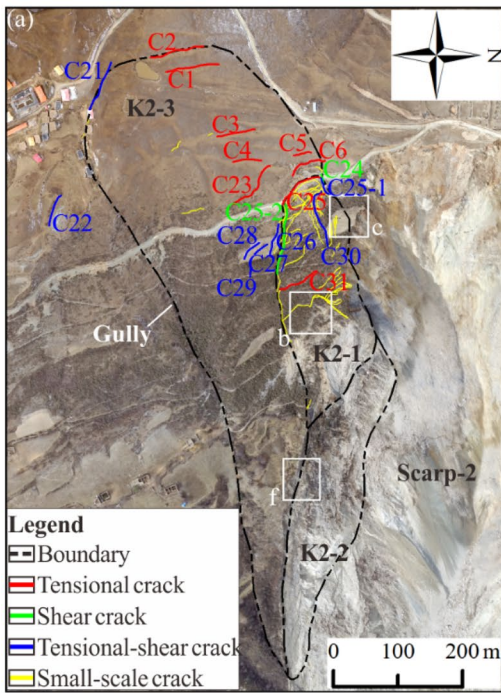
Crack	Mechanical Property	Property				
		Strike (°)	Dip angle (°)	Length (m)	Width (cm)	Depth (cm)
C6-1	Shear	60	105	23	5	36
C7	Tension	310-345	40-75	23	9	50
C8	Tension	345	55	84	15-22	27-45
C9	Tension	3	80	92	21	52
C9-1	Tension	5	85	68	10-35	35-70
C10	Tension	350-15	70-105	176	54	125
C10-1	Tension-shear	300	45	18	20-45	30-48
C11	Tension-shear	5	/	118	7	66
C12	Tension-shear	3	85	117	4-18	15-37
C13	Tension-shear	358	91	31	3-12	20-37
C14	Tension	6	90	43	5-20	18-45
C15	Tension	350-15	70-105	64	10-23	35-50
C16	Tension	3	85	65	18-35	40-65
C16-1	Tension-shear	310	45	13	8	52
C17	Tension	358	86	48	5-20	18-45
C18	Tension	340-10	68-95	68	8-27	24-58
C19	Tension	359-10	88-105	133	5-16	18-32
C20	Shear	98	100	15	5-8	17-30
C32	Tension	76	105	39	35	62
C32-1	Tension	22	113	0	21	115
C33	Tension-shear	91	106	80	15	65
C33-1	Tension-shear	151	145	46	25-53	85

Fig. 4 Surface crack mapping results for K1: **a** characteristics of cracks on K1, **b** and **k** multiple small-scale and dense imbricate cracks distributed near the free surface, followed by several larger-scale transverse cracks, such as **c–e** C10, **f** C12, **g** C19, **h** C11, and **i** C32 and C32-1, and **j** a graben-like trough with maximum width of ~1.7 m, and a head scarp up to ~4.5 m high on the west side of this graben

Geological structures

In addition to regional fault F1 (as shown in Fig. 1), a series of local geological structures that are otherwise difficult to detect on the surface can be determined near the rockslide areas by the geophysical survey. As shown in Fig. 9, several representative profiles obtained by the geophysical survey (MSM and AMS) have been made. Several faults or fracture zones can be inferred from the MSM profiles shown in Fig. 9. Reflectors approximately oriented to S–N (i.e., profile 1–1′ in Fig. 9), consisting of one segment of lower resistivity and two segments of lowest resistivity as indicated by blue and light green colors, respectively, in the AMS profile (Fig. 9a), are

interpreted to be three steep faults or fracture zones that are named as F1, F2, and F3. In particular, F2 daylights at the surface in the same area (Fig. 10a) as a mapable feature of the AMS profile and field investigation. Among these faults or fracture zones in profile 1–1′, F3 is relatively small in scale and exhibits a trend of northward dip, while F1, dipping to N, and F2, dipping to S, are larger in scale, thereby causing a wider range of heavily fractured rock on the south side of F2 (Fig. 9a). Other, lower resistivity zones, shown in light green along profile 2–2′ by AMS, indicate that K2 is located in an area with larger-scale steep faults or fracture zones (named F4), mainly dipping to W (Fig. 9b). Moreover, on the right side of profile 2–2′,

| Crack	Mechanical Property	Property				
		Strike (°)	Dip angle (°)	Length (m)	Width (cm)	Depth (cm)
C1	Tension	352	75	83	5-8	19-51
C2	Tension	350	65	86	11	16-22
C3	Tension	349	68	60	7	40
C4	Tension	355	60	45	3	20
C5	Tension	350	65	29	5	18
C6	Tension	300-345	35-75	64	18	20
C21	Tension-shear	115	/	82	5-13	17-25
C22	Tension-shear	107	/	52	5-8	13-22
C23	Tension	314	45	91	3-7	23
C24	Shear	71	85	13	22	49
C25	Tension	330	78	79	45	85
C25-1	Tension-shear	70	80	32	12	26
C25-2	Shear	95	79	111	15-35	45
C26	Tension-shear	105	91	50	27	70
C27	Tension-shear	143	70	26	5	36
C28	Tension-shear	135	72	35	4	35
C29	Tension-shear	92	81	13	11	45
C30	Tension-shear	70	46	97	5-26	65
C31	Tension	336	65	67	15	50
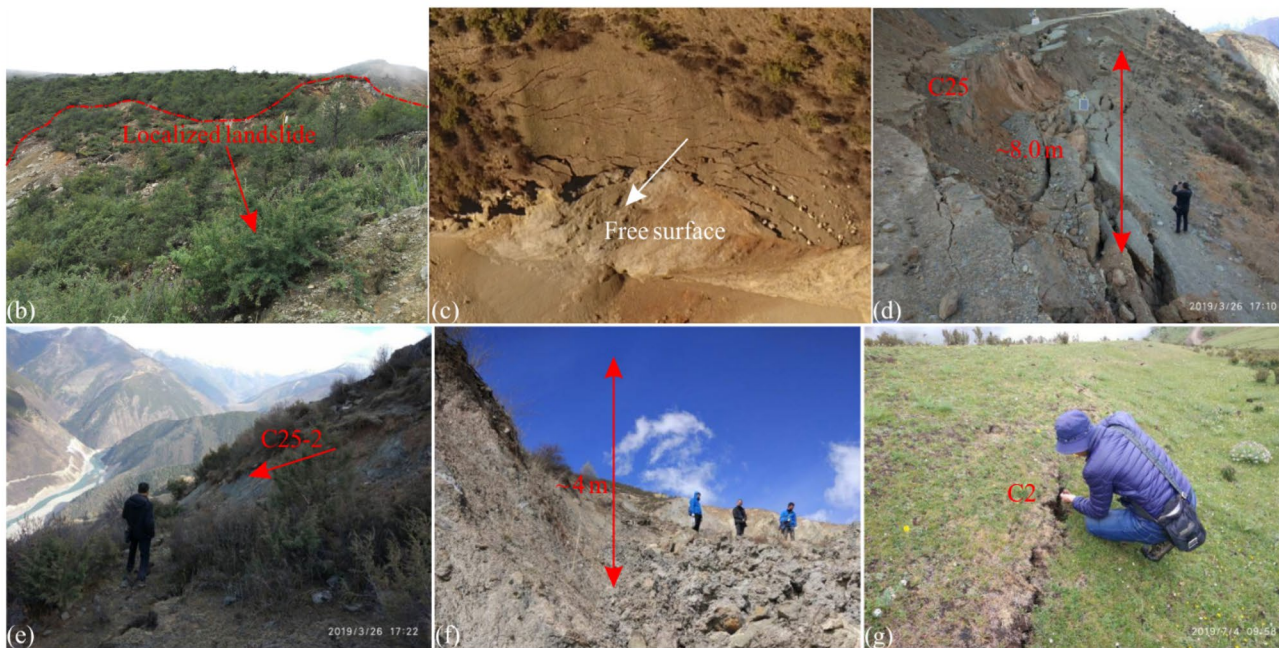
Fig. 5 Surface crack mapping results for K2: **a** characteristics of cracks on K1, **b** a localized landslide developed in the middle of K2 induced by several dense arc-shaped NS-striking cracks, **c** dense arc-shaped cracks on the north side of K2 that fracture the rock masses and result in the unstable blocks of K2 gradually deforming and disintegrating toward the free surface, **d** larger-scale crack C25 forming a scarp, **e** a derivative crack of C25 (named C25-2) along the EW strike, **f** a scarp with a maximum dislocation height of ~4 m, and **g** a tensile crack C2 distributed on the upper part of K2

several lower resistivity zones, such as zones in profiles 3–3' (Fig. 9c) and 7–7' (Fig. 9d), are also interpreted as faults/fracture zones. These faults/fracture zones have similar distribution characteristics to F4, and therefore are inferred as a northward extension of F4.

As such, based on the geophysical survey results in this study, many faults/fracture zones were identified. Additionally, folds are well-developed in the rockslides area. These undesirable geological structures cut through the rock masses constituting the rockslides and result in visible tectonic lens. As shown in Fig. 10b, in the area around the tectonic lens, the rock masses are described by extreme fragmentation, brecciation, and mylonitization subjected to compression due to active tectogenesis.
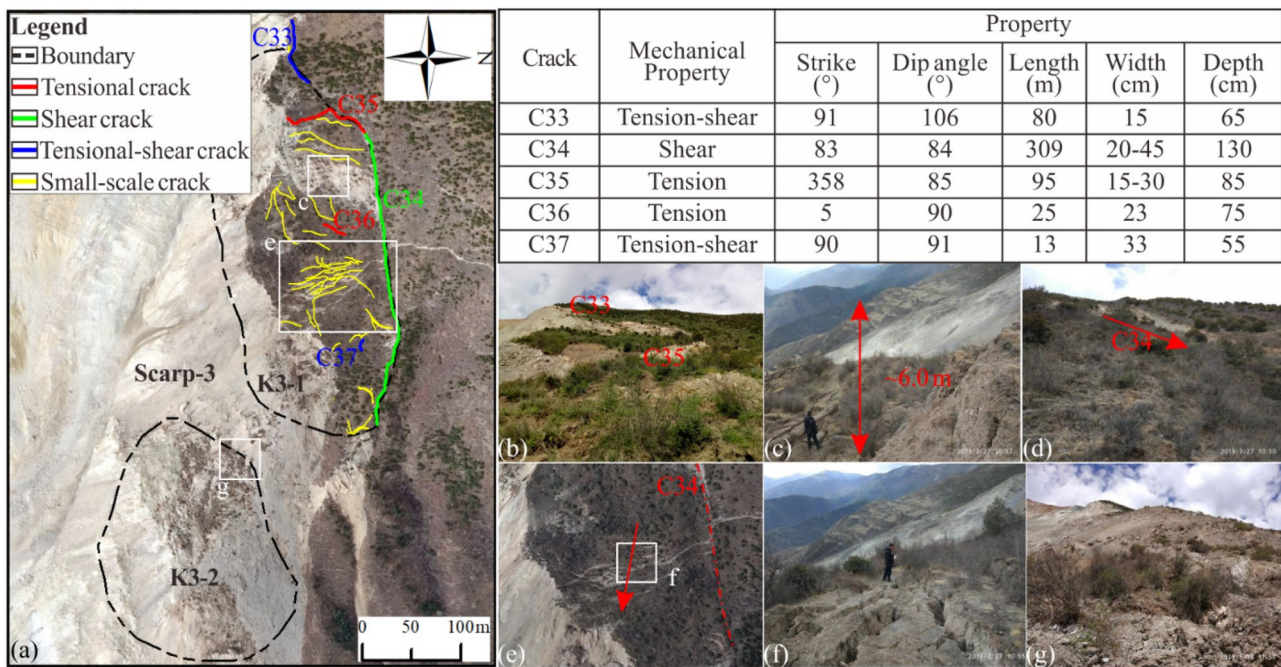
Fig. 6 Surface crack mapping results for K3: **a** characteristics of cracks on K3, **b** and **c** many arc-shaped tensile cracks distributed at the upper part of K3, causing the rock mass to be pulled apart and thus resulting in the formation of visible scarp, **d** a remarkable shear crack C34 on the left side of K3 defined the boundary of K3, **e** and **f** bulging cracks distributed in the middle of K3 due to the continuous eastward expansion of the sliding block under impeded by the front rock masses, and **g** a back scarp of K3

Characteristics of rock masses

High-grade metamorphism and corresponding deformation associated with polyphase tectogenesis are known to have significant influences on landslides by altering rock mass strength. Generally, our rock fracture investigation indicates that the revealed rock masses are likely to be affected by faults, fracture zones, and folds, which are denoted by the relatively small RQD (marked in Fig. 7) and low fissure coefficient (calculated by Zhang et al. 2020b). It is interpreted that the recorded RQD values and agitated fluctuations of P-wave velocities (Fig. 7) indicate greatly varying degrees of fracturing across different localities. Specifically, as a common bedrock in the rockslide areas, gneiss is fractured by foliation with orientation of 150°–220°∠35°–62° (Zhang et al. 2020b). As the two most distinctive rock masses in the rockslide areas, serpentinite and carbonaceous rocks (e.g., carbonaceous slate) can be described as crumbly granular and clay texture, respectively, involving lower RQD values and P-wave velocities (Fig. 7), thus strongly imparting the kinematic release ability.

Investigation of activity features

Recorded overall deformation features

Figure 11 presents the monthly average magnitudes and directions of displacement since the installation of the GNSS monitoring instruments. Some basic information on these GNSS monitoring points is presented in Table 2. From Fig. 11, the GNSS monitoring instruments clearly record various magnitudes of deformation at the different rockslide areas, illustrating relative inactivity of K1 and higher activity of K2 and K3. Except for the average displacement of G6 (~ 20.6 mm/month) in K1-4 and G7 (71.2 mm/month) in K1-5, most GNSS points in K1 record relatively lower-level average displacement ranging from ~ 3.9 mm/month to ~ 11.6 cm/month (Fig. 11 and Table 2). In comparison, greater displacement magnitudes recorded in K2 and K3 are very common, especially for the GNSS points in K2-1, K2-2, and K3-1, showing values greater than ~ 40 mm/month, and even up to ~ 1219.4 mm/month (Fig. 11 and Table 2). Further, the recorded data from K2-1 shows that the average displacement decreases toward the toe, from ~ 504.8 at G19 to ~ 46.9 mm/month at G14, with an approximately decreasing trend with decreasing elevation (Fig. 11). In contrast, GNSS monitoring results on K3-1 show a reverse trend compared with K2-1. As shown in Fig. 11, the average displacement generally increases toward the toe from ~ 81.7 at G28 to ~ 167.0 mm/month at G24. In addition, according to Fig. 11, we can easily find that the kinematic direction for most GNSS monitoring points is toward the failure area.

Recorded deformation evolution features

Displacement–time curves are used to emphasize the response processes under external disturbances (such as rainfall and unloading in the rockslide areas). Figures 12–14 present the cumulative displacement plots of GNSS and crack meters. Due to the larger number of monitoring points in K1, the monitoring results for the absolute and relative surface deformations with monitoring times less than 1 year and more than 1 year are shown in different graphs, enabling the change characteristics of displacement processes in K1 to be more concise.

Table 1 Subdivided eleven subdomains and controlled boundaries

Area	Subdomain	Boundary
K1	K1-1	Upper boundary: C9, C9-1, C10, C17, and C14 with ~500 m long
		Lower boundary: Upper part of the cliff on Scarp-1 with ~480 m long
		Left boundary: Downward extending of crack on the left side with ~60 m long
		Right boundary: Downward extending of crack on the right side with ~160 m long
	K1-2	Upper boundary: C12 and C13 with ~330 m long
		Lower boundary: Cracks of K1-1 on the back scarp with ~320 m long
		Left boundary: Extending of C14
		Right boundary: Downward extending of crack on the right side
	K1-3	Upper boundary: C19 with ~180 m long
		Lower boundary: Cracks of K1-1 on the back scarp with ~165 m long
		Left boundary: Extending of crack on the left side
		Right boundary: Extending of crack on the right side
	K1-4	Upper boundary: Extending of crack with ~65 m long
		Lower boundary: Upper part of the cliff on Scarp-1 with ~80 m long
		Left boundary: Extending of C20
		Right boundary: Extending of crack on the right side
	K1-5	Upper boundary: Extending of C32 with ~65 m long
		Lower boundary: Upper part of the cliff on Scarp-1 with ~120 m long
		Left boundary: Extending of C32-1 with ~70 m long
		Right boundary: Upper part of the cliff on Scarp-1 with ~85 m long
	K1-6	Upper boundary: Extending of C11 with ~125 m long
		Lower boundary: Cracks of K1-2 on the back scarp with ~220 m long
		Left boundary: Downward extending of crack on the left side
		Right boundary: Downward extending of crack on the right side
K2	K2-1	Upper boundary: Extending of crack C25 with ~120 m long
		Lower boundary: Dislocated minor scarp on Scarp-2 with ~400 m long
		Left boundary: Extending of crack on the left side
		Right boundary: Downward extending of crack C25-2 with ~390 m long
	K2-2	Upper boundary: Dislocated minor scarp on Scarp-2 with ~180 m long
		Lower boundary: Dislocated minor scarp on Scarp-2 with ~600 m long
		Left boundary: Extending of dislocated minor scarp on Scarp-2
		Right boundary: Dislocated minor scarp on Scarp-2 with ~490 m long
	K2-3	Upper boundary: C2 and C21 with ~310 m long
		Lower boundary: Dislocated minor scarp of K2-1 and K2-2 with ~800 m long
		Left boundary: Extending of crack on the left side
		Right boundary: Narrow gully

Table 1 (continued)

Area	Subdomain	Boundary
K3	K3-1	Upper boundary: C33 and C35 with ~120 m long
		Lower boundary: Dislocated minor scarp on Scarp-3 with ~380 m long
		Left boundary: Downward extending of crack C34 with ~500 m long
		Right boundary: Dislocated minor scarp on Scarp-3
	K3-2	Upper boundary: Dislocated minor scarp on Scarp-3 with ~90 m long
		Lower boundary: Dislocated minor scarp on Scarp-3 with ~210 m long
		Left boundary: Extending of dislocated minor scarp on Scarp-3
		Right boundary: Extending of dislocated minor scarp on Scarp-3

From the perspective of deformation evolution over time, a period of transient yet very rapid deformation, which is always observed at the onset of deformation monitoring but subsequently disappears, is recorded in some monitoring points that were installed immediately after the second rockslide event in November 2018 (Figs. 12–14). Such deformation characteristics are likely closely associated with the dramatic unloading caused by the successive rockslide events. Subsequently, the deformation response process transforms into that of progressive failure caused by time-dependent strength degradation under external disturbance, including rainfall and unloading at the top of the rockslides. When the first rainy season after the successive landslides started (i.e., May to October 2019), different deformation processes are observed with respect to different areas. For K1, the change of deformation at all monitoring points in this area is mostly unapparent (Fig. 12), suggesting that this area is not sensitive to rainfall or that there is insufficient rainfall at this stage to trigger larger deformation. However, from the monitoring points on K2 (Fig. 13), it is evident that rainfall strongly affected the deformation in this area, which presents a relatively large deformation rate over time. In particular, the GNSS monitoring results in K2-1 and K2-2 show that the deformations in these two subdomains seem to be "excited" and continually increase for a relatively long time at high rates. In contrast, for K3, the first rainy season results only in minor stepped or graded cumulative displacement, and is subsequently followed by a gentle trend over a relatively long period. Before the second rainy season, unloading at the top of rockslides has been completed, which effectively alleviates the ongoing deformation. As shown in G9, it experiences a reduction in deformation from December 2019 to April 2020 (Figs. 12a, b). In the second rainy season (i.e., May to November 2020), the most prominent observations for K1 are noted as follows (Fig. 12). (i) Rainfall is still nearly ineffective in terms of deformation except for K1-5. (ii) For K1-5, where serpentinite is widely distributed, a surge of movement from 80 to 920 cm is recorded during June to August 2020, showing the characteristics of brittle failure, which is then followed by the deformation rate returning to a lower state. It should be noted that such deformation phenomenon does not occur in the first rainy season. Therefore, it can be inferred that a certain extent of accumulative degradation

of physical–mechanical properties for serpentinite is a prerequisite for remarkable brittle deformation. In terms of K2, it can be seen from the monitoring curves (Fig. 13) that the second rainy season has little impact on K2-3 but again increases the deformation of K2-1 and K2-2, which is associated with the local instability at monitoring point G13. Moreover, as shown in Fig. 14, the cumulative displacement curves indicate that the motion of K3 in the second rainy season is not constant, but rather stepped or graded, which is illustrated by rapid displacements over a shorter period followed by a lower rate. These deformation characteristics in the second rainy season are similar to that of the first rainy season. The only difference is that the stepped or graded magnitude in the second rainy season is much larger than that in the first rainy season, especially for K3-1.

Deformation-failure features from multi-phase field observations

After the completion of unloading at the top of the rockslide, the deformation-failure evolution characteristics for these rockslides are presented in Figs. 15–17 according to our multi-phase field observations. Generally, the findings coincide well with the monitoring results. For K1, the deformation trend of the unloading area is effectively alleviated, and no new cracks are found in the subsequent observations. However, significant deformation is in the two spoil landfills at the front part of K1-1 (Figs. 15a–c) with a total projected area of ~4135 m^2 and a volume of ~15 × 10^4 m^3. As shown in Fig. 15b, a large number of tension and shear cracks develop in this area, and the maximum vertical offset is ~4 m. In addition, for K1-4 and K1-5 distributed with serpentinite, failure and significant deformation, as well as new dense systems of cracks, are observed. As shown in Figs. 15d–e, a crack formed after October 2019 has coalesced at the time of our investigation in March 2020, consequently resulting in failure of the front part of K1-4. As for K1-5, due to the intrinsic weathering-prone attribute of serpentinite, the deformation-failure range is constantly expanding and extending to the top, as evidenced by the newly formed crack, which is 0.9 m in depth and 10 m in length (Figs. 15f–g), and is gradually propagating toward K1-4 (Fig. 15h).

The most remarkable deformation-failure phenomenon in K2 occurs in K2-1. The original C25 distributed at the top of K2-1
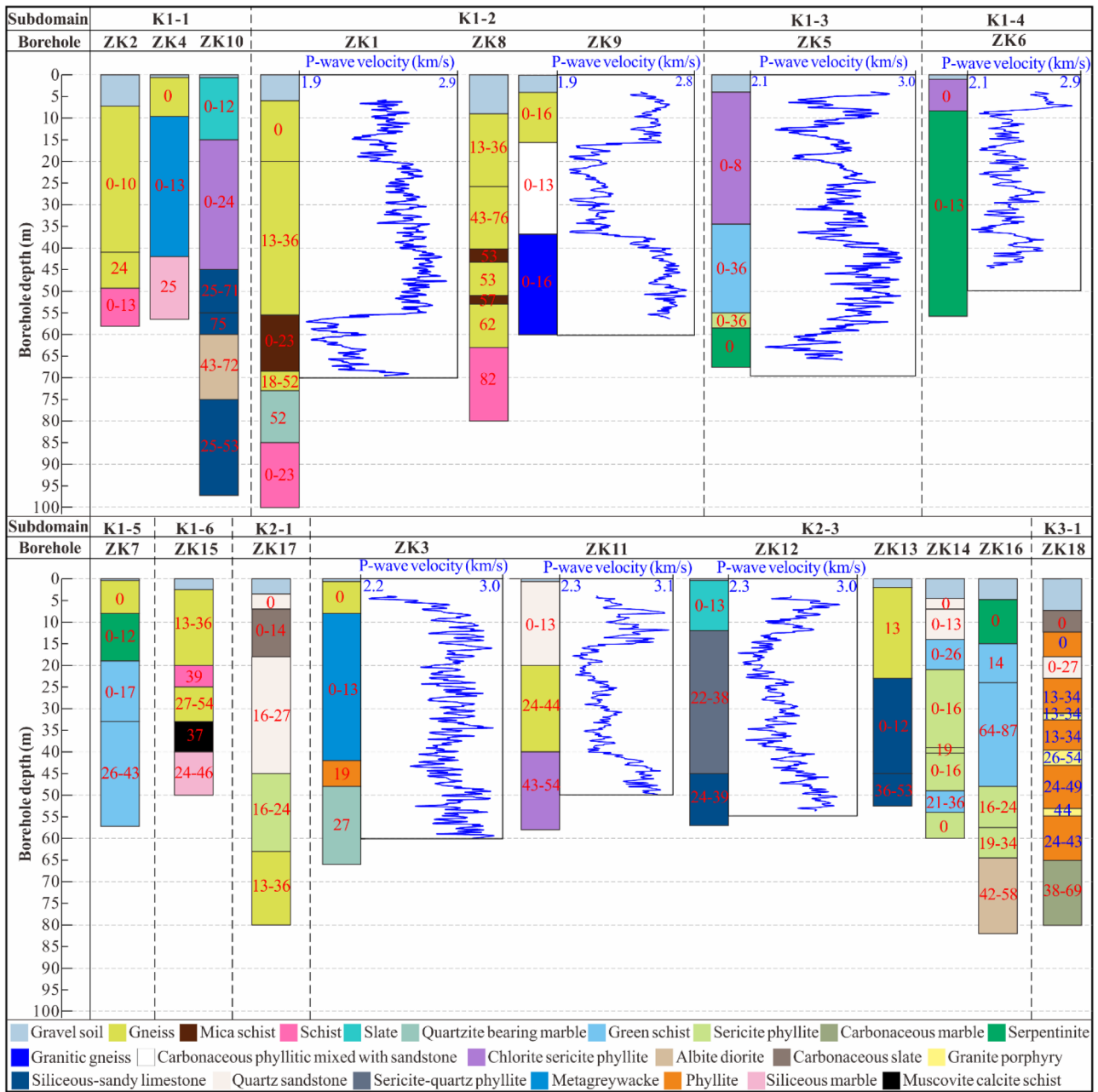
Fig. 7 Characteristics of the rock masses in the boreholes. The values of RQD are marked in the catalog of each core (unit: %). The sonic logging of P-wave for ZK1, ZK3, ZK5, ZK6, ZK9, and ZK11 is illustrated on the right side of the borehole catalog

has been excavated, but the investigation results show that a new arc-shaped crack is generated at the original position of C25 (Fig. 16a). This newly formed crack is in a state of continuous propagation as indicated by Figs. 16a–c. Based on our investigation in March 2020 (Figs. 16b, d–f), this newly formed crack has extended to a width of 0.2–0.3 m, with a depth of 0.7 m, and connected with the pre-existing shear crack (C25-2). Additionally, at the lower part of K2-1, a bulging crack is visible (Fig. 16e). These features imply that the boundary of K2-1 has been formed as defined by the aforementioned cracks. Moreover, as shown in Fig. 16f, there is a band of groundwater seepage in the highly

weathered carbonaceous slate near the toe of K2-1. Concurrently, due to the saturation and softening caused by the continuous infiltration of groundwater, the highly weathered carbonaceous slate more likely serves as the main failure surface of K2-1 (Fig. 18a), which is confirmed by the severe hole sticking and slurry leakage occurring at a depth of 15 m in ZK17 during drilling.

The deformation-failure features for K3-1 are presented in Fig. 17. It can be seen that the deformation and failure are becoming increasingly active via step-by-step gradual disintegration, as indicated by the well-developed multistage sub-cracks
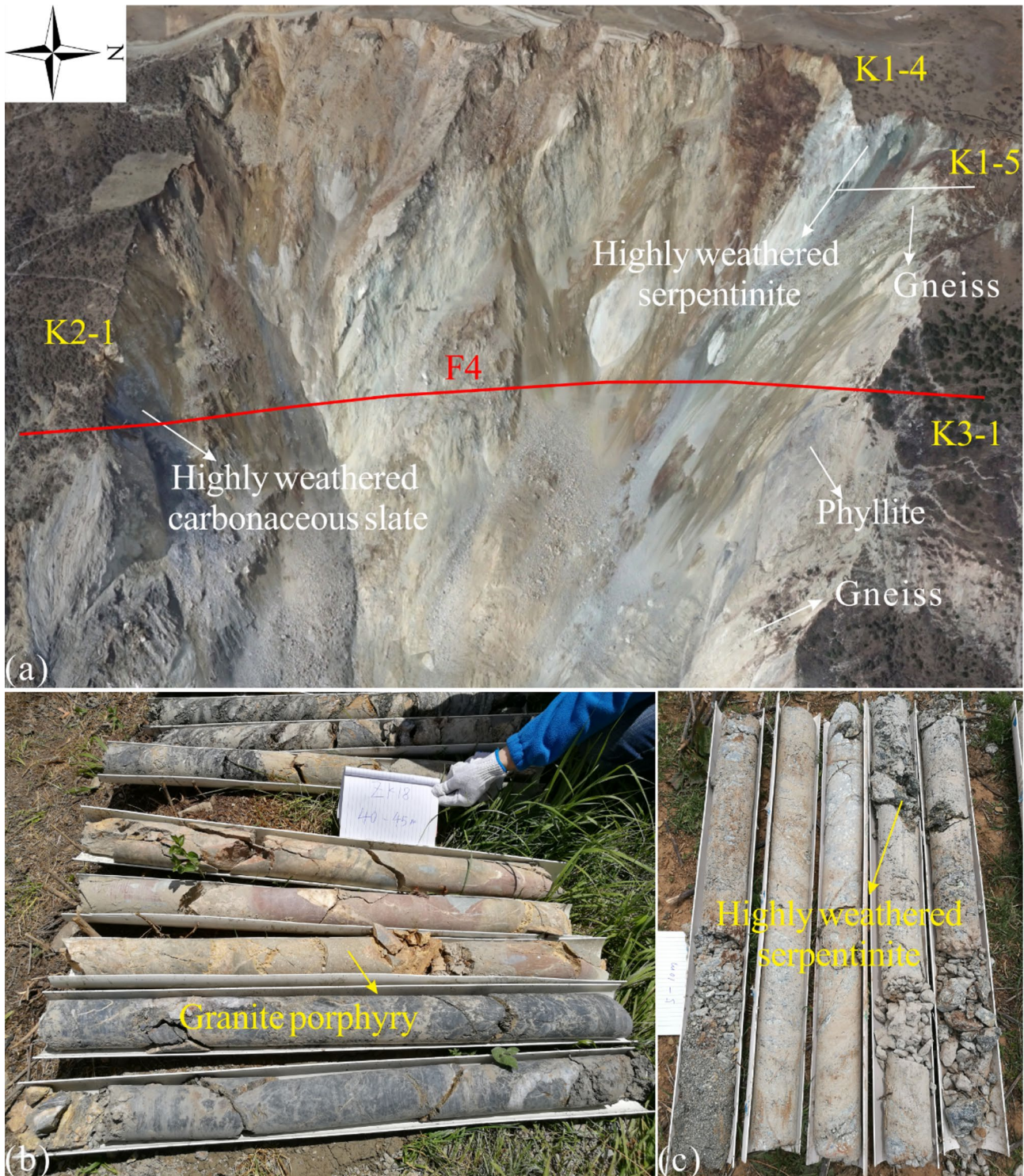
Fig. 8 Exposed special geo-structures near the landslide scar: **a** daylighting special rock masses and interpreted F4, **b** exposed granite porphyry in ZK18, and **c** exposed serpentinite in ZK16

(Fig. 17a) and local collapse at the toe of the highly weathered gneiss (Fig. 17b). According to the borehole core of ZK17, the rock undergoes tectogenesis and is brecciated at the depth of 19–21 m (Fig. 18b), which is inferred as the potential failure surface of K3-1.

Discussion

Influence of geo-structure on rockslide deformation and failure
It is common for unstable rockslides to develop near a landslide scar, such as in the Randa (Willenberg et al. 2008a, b), Xinmo
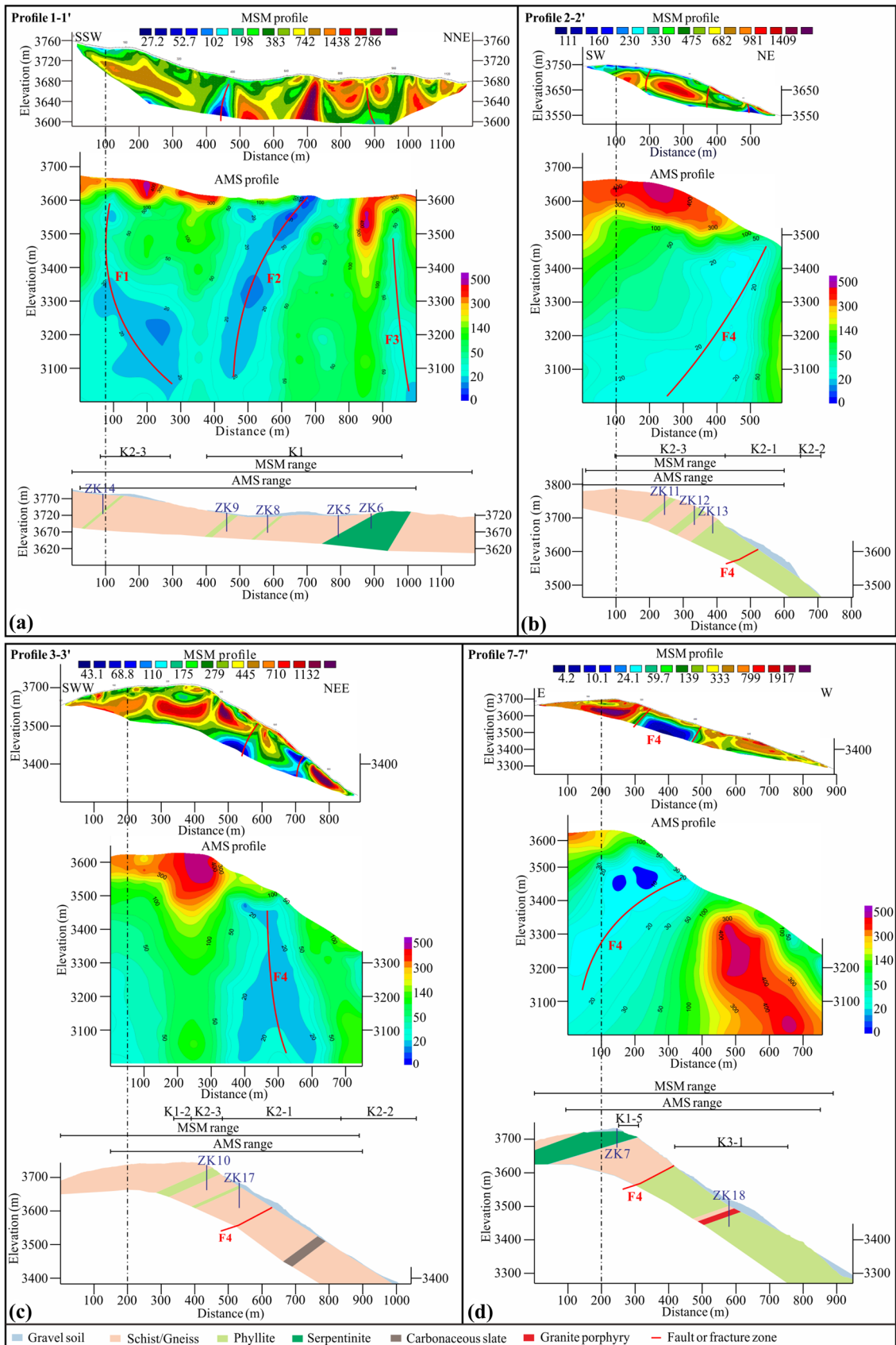
Fig. 9 Geophysical survey results by MSM and AMS and related geological profiles for **a** profile line 1–1′, **b** profile line 2–2′, **c** profile line 3–3′, and **d** profile line 7–7′. The profile lines are taken from Fig. 7

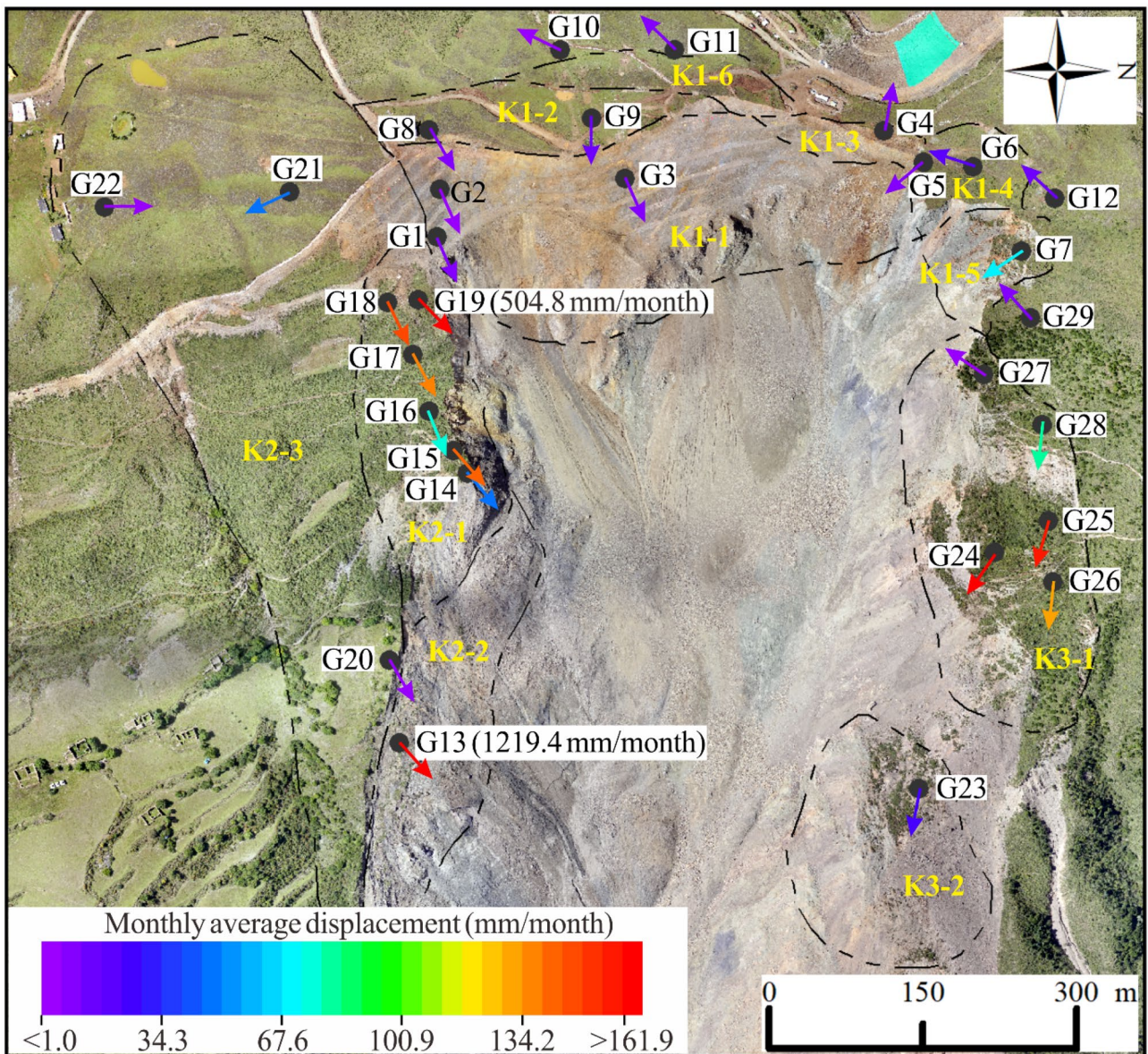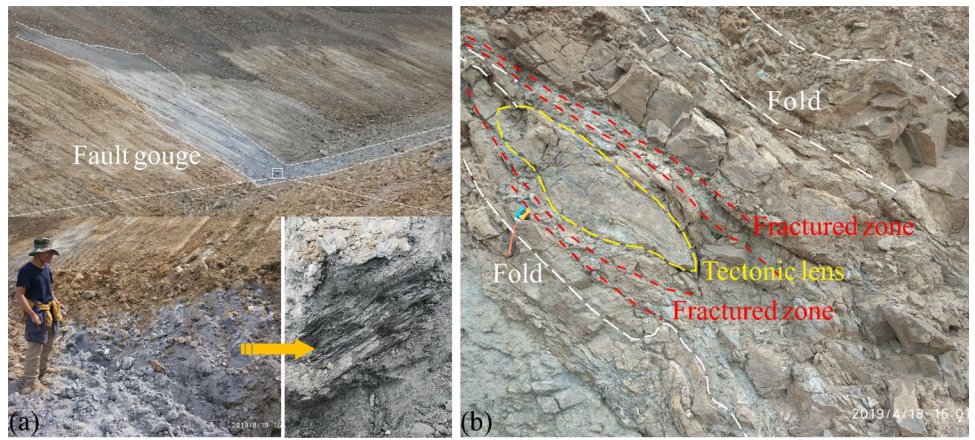**Fig. 10** Geological structures observed in the field: **a** fault gouge and **b** fold

Fig. 11 Monthly average displacement recorded by GNSS

Table 2 Information and GNSS monitoring results. The vertical displacement is positive upward. The deadline for all monitoring data statistics is October 28, 2020

Point	Area	Horizontal displacement (mm)	Vertical displacement (mm)	Total displacement (mm)	Average displacement (mm/month)	Dip (°)	Stratum	Installation time (year/month/day)
G1	K1-1	26.8	−37.6	46.2	10.8	66	$P_t xn^a$	2020/6/22
G2	K1-1	14.4	1.5	14.5	3.9	66	$P_t xn^a$	2020/7/8
G3	K1-1	21.3	−23.2	31.5	10.6	66	$P_t xn^a$	2020/7/31
G4	K1-3	164.3	−39.6	169.0	9.5	280	$P_t xn^a$	2019/5/16
G5	K1-4	26.7	1.2	26.7	9.0	140	$P_t xn^a$	2020/7/31
G6	K1-4	476.1	64.2	480.4	20.6	198	$\varphi_{\omega 4}$	2018/11/28
G7	K1-5	982.3	−781.5	1255.2	71.2	146	$\varphi_{\omega 4}$	2019/5/18
G8	K1-2	71.6	−113.3	134.0	7.6	60	$P_t xn^a$	2019/5/15
G9	K1-2	222.1	−268.3	348.3	14.6	90	$P_t xn^a$	2018/11/11
G10	K1-6	70.2	41.7	81.7	4.7	206	$P_t xn^a$	2019/5/22
G11	K1-6	174.8	103.0	202.9	11.6	224	$P_t xn^a$	2019/5/22
G12	/	196.9	110.6	225.9	12.8	223	$P_t xn^a$	2019/5/19
G13	K2-2	18,454.3	−10,795.2	21,379.8	1219.4	48	$P_t xn^a$	2019/5/21
G14	K2-1	137.3	−127.4	187.4	46.8	50	$P_t xn^a$	2020/6/30
G15	K2-1	2243.9	−997.3	2455.6	140.9	49	$P_t xn^a$	2019/5/24
G16	K2-1	1156.8	−636.0	1320.1	75.9	68	$P_t xn^a$	2019/5/25
G17	K2-1	1832.0	−1451.7	2337.4	134.3	62	$P_t xn^a$	2019/5/25
G18	K2-1	2784.5	−2240.1	3573.7	149.3	64	$P_t xn^a$	2018/11/10
G19	K2-1	1690.4	−1334.7	2153.8	504.8	46	$P_t xn^a$	2020/6/22
G20	K2-3	87.6	6.3	87.8	5.0	60	$P_t xn^a$	2019/5/25
G21	K2-3	657.0	−526.1	841.7	47.8	155	$P_t xn^a$	2019/5/19
G22	K2-3	46.2	−23.4	51.8	2.9	0	$P_t xn^a$	2019/5/19
G23	K3-2	317.0	−345.0	468.5	26.9	101	$P_t xn^a$	2019/5/25
G24	K3-1	3482.2	−1962.5	3997.1	167.0	125	$P_t xn^a$	2018/11/10
G25	K3-1	1863.9	−1551.0	2424.8	158.1	106	$P_t xn^a$	2019/7/26
G26	K3-1	2102.6	−1580.8	2630.6	130.7	96	$P_t xn^a$	2019/3/4
G27	K3-1	83.2	18.3	85.2	5.6	214	$P_t xn^a$	2019/7/26
G28	K3-1	1273.3	−650.9	1430.0	81.7	96	$P_t xn^a$	2019/5/22
G29	/	115.6	41.3	122.7	8.1	228	$P_t xn^a$	2019/7/29

(Wang et al. 2020), and Hongshiyan landslides (Li et al. 2019a, b), which are closely associated with landslide-induced unloading and rebounding processes. In our view, although this process initiates new cracks and causes the pre-existing cracks to propagate further due to the redistribution of the stress regime, such effects caused by unloading and rebounding are only transient. This is demonstrated in the present study by the response characteristics observed from the monitoring curves with periods of short-lived yet very rapid deformation for several monitoring points installed immediately after the second rockslide event, including G6, G9, G18, and G24 (Figs. 12–14). However, the subsequent development and evolution of the unstable rock blocks are intensely related to the daylighting geo-structure. In this section, the influence of geo-structures on deformation and failure of rockslide areas are discussed.
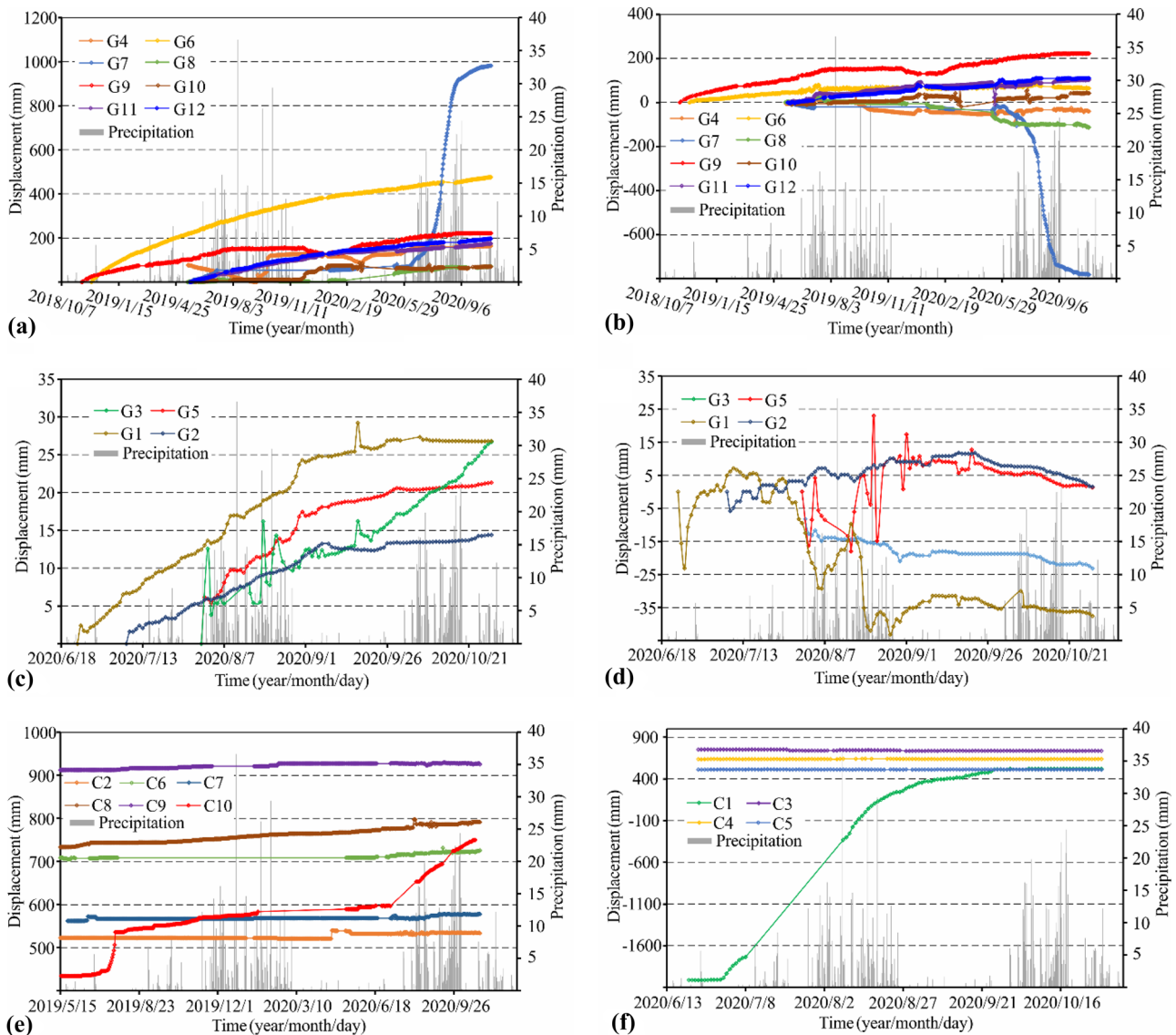
Fig. 12 Displacement and precipitation versus time curves on K1: **a** and **c** horizontal displacement versus time monitored by GNSS, **b** and **d** vertical displacement versus time monitored by GNSS, and **e** and **f** relative displacement–time curves obtained from extensometer. The vertical displacement is positive upward

Regionally, the rockslide areas are subjected to polyphase active tectogenesis (Fan et al. 2019; Li et al. 2019a, b; Zhang et al. 2020b), resulting in the continuous deformation and metamorphism of rock masses. Several adverse geological structures, including faults, folds, and fracture zones, are well-developed in this area and closely associated with the fragmentation, brecciation, and mylonitization of rock masses. Thus, certain adverse aspects from these geological structures are crucial to the development of through-going failure surfaces for rockslides, such as the alteration of the strength of the rock masses associated with faulting (Brideau et al. 2019; Stead and Wolter 2015) (e.g., the widespread fragment rock masses in K2-1, K1-4, and K1-5) and fault-related hydrogeology (Martins-Campina

et al. 2008) (e.g., the continuous infiltration of groundwater in K2-1).

From the lithology and rock fracture data shown in Fig. 7, it can be concluded that due to the varying degree of metamorphism, deformation, and weathering extent, the rock masses in the rockslide areas can be characterized by the wide and interbedded spatial distribution of various lithologies with extremely heterogeneous qualities. Such mutually embedded structures lead to many blocks not sliding despite apparent deformation, such as K1-5, because the front parts of these blocks are supported by better quality rock masses. Furthermore, according to our investigation results of the characteristics of rock masses ("Characteristics of rock masses" section)
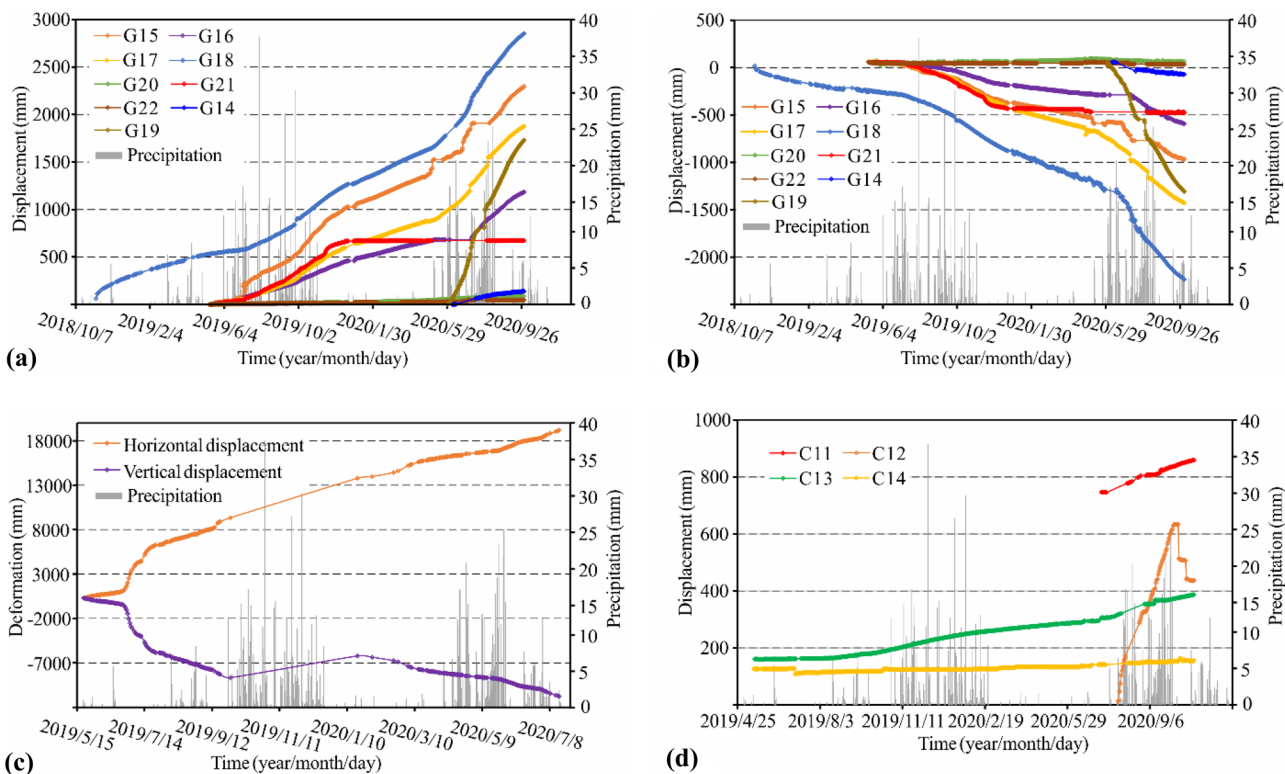
Fig. 13 Displacement and precipitation versus time curves on K2: **a** and **b** horizontal and vertical displacement versus time monitored by GNSS, respectively, **c** displacement–time curves obtained from G13, and **d** relative displacement–time curves obtained from extensometer. The vertical displacement is positive upward

and the activity features ("Deformation-failure features from multi-phase field observations" section), the deformation-failure-prone structures of the rockslide area are predominately composed of serpentinite and carbonaceous slate. It is expected that when the progressive accumulative deterioration of physical–mechanical properties of the serpentinite reaches a certain degree, a sudden and remarkable fragile failure may occur, and rainfall is expected to enhance this deterioration process, as shown by the result of monitoring point G7. As for carbonaceous slate, under the effect of water-induced infiltration, this highly weathered material can transform into a soft zone of saturated muddy clay, thereby resulting in a great reduction in strength. This is the main reason for the deformation of K2-1 appearing highly sensitive to rainfall.

Geological evolution model based on observations

The interpretation of the underlying geological evolution model can facilitate the identification of rockslide changes (Rose and Hungr 2007; Zhang et al. 2018a). Therefore, in this section, the potential evolution models for four subdomains with active deformation (K1-4, K1-5, K2-1, and K3-1) are presented for further numerical analyses in the future.

First, in K1-4 and K1-5, where serpentinite is widely distributed, the deformation-failure range generally continues to expand

backward, which is manifested in the continuous initiation, propagation, and coalescence of new cracks at the top of both areas (Fig. 15d–h). However, because K1-4 and K1-5 have different internal structures, their geological evolution models vary. As shown in Fig. 8a, the rock mass in K1-4 primarily consists of serpentinite. Thus, cracks propagate more easily due to brittle fracturing of the serpentinite. However, the middle and upper parts of K1-5 are mainly composed of serpentinite with concave vein-like distribution, while the lower part of K1-5 is mingled with relatively intact gneiss (Fig. 8a). Thus, deformation toward the free surface caused by the strength degradation of serpentinite in K1-5 is effectively impeded by the gneiss, which thereby leads to only the shallow layers descending progressively from the middle part to the upper part of K1-5 (Fig. 15g).

As for K2-1, combined with the overall deformation feature that gradually increases from the toe to the top (Fig. 11 and Table 2) and the observed bulging crack at its front part (Fig. 16), we can infer that the deformation-failure behavior, with bearing on these features, is characterized by "back-pushing" of en masse slide. This implies that the front part of K2-1 is able to act as the locking section and thereby likely to both support the overlying rock mass and synchronously impede the deformation of the upper part of K2-1. Further, the extremely "mature" boundary and dramatic groundwater seepage indicate that this subdomain has the potential to fail.
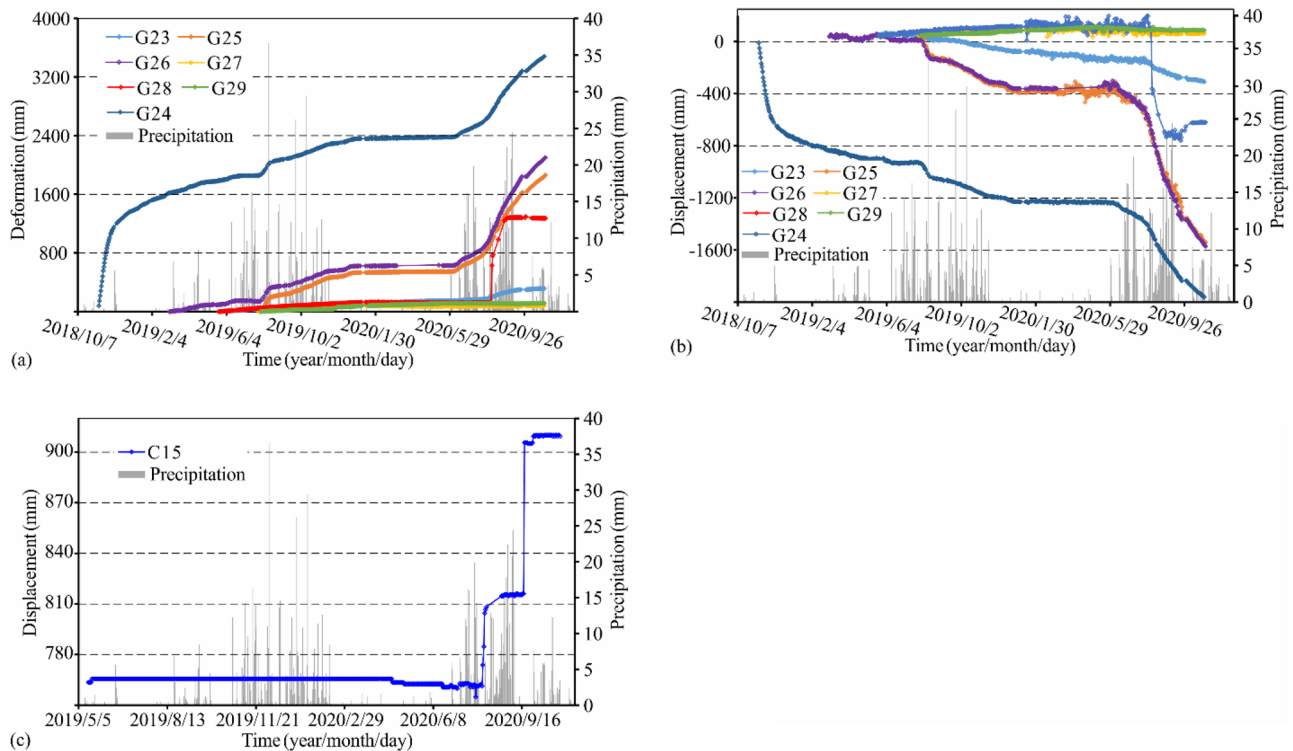
Fig. 14 Displacement and precipitation versus time curves on K3: **a** and **b** horizontal and vertical displacement versus time monitored by GNSS, respectively, and **c** relative displacement–time curves obtained from E15. The vertical displacement is positive upward

For K3-1, due to the better rock mass integrity existed in the deeper layers (Figs. 7 and 8b), the gradually decreasing overall deformation trend is illustrated from the toe toward the top of the unstable block (Fig. 11 and Table 2), thereby showing multistage superficial collapse. The underlying evolution model is proposed to be "fore-pulling" of retrogressive superficial collapse in a progressive way with a lesser possibility of deep-seated failure.

Uncertainties

This study aimed to analyze the geological characteristics and evolution models for unstable rockslides based on existing and available data. However, the broken rock masses and the complex lithological distribution related to the unique geological background have generated uncertainties for analyzing the unstable rockslides near the Baige landslide scar.

The extent of the potentially unstable rockslide areas detected in this study is primarily identified through displacement measurements and field observations. However, when encountering complex geological conditions, the interpretation of such boundaries can often be ambiguous, because the changing geometrical boundaries and rock mass structures of moving rockslides driven by complex internal processes often give rise to dynamic changes of the deformation areas (Rose and Hungr 2007).

It is well known that strata attached to serpentinite belong to failure-prone geological structures, but research on the mechanical properties of this rock type for the study of landslide evolution is highly preliminary. Our presented understanding is only of serpentinite vulnerability to brittle fracture and weathering, lacking further revelation of the underlying mechanism leading to failure. In addition, some serpentinite distribution areas in this study area are not included in this analysis, such as the south side of K2 where ZK16 is located. Such a presence of serpentinite likely indicates a further unstable rockslide area on the south side of K2, in which case, the narrow gully on the south flank of K2 would not be the true south boundary. This inference can be further confirmed by crack C22 within this area (Fig. 5a) and the deformation monitoring using the multi-temporal InSAR conducted by Xiong et al. (2020).

Moreover, the geophysical survey employed in this study interprets several faults or fracture zones, among which F2 is exposed (Fig. 10a). However, the existence of the remaining faults or fracture zones remains debatable without the possibility of verification. In addition, even though the rock cores are cataloged from a total of eighteen boreholes, strata in many of the crucial subdomains, such as the front part of K2-1, are not able to be completely revealed due to the limitation of topography on drilling, which constrains both the data resolution and the detailed geo-structure. Furthermore, it should be noted that the potential
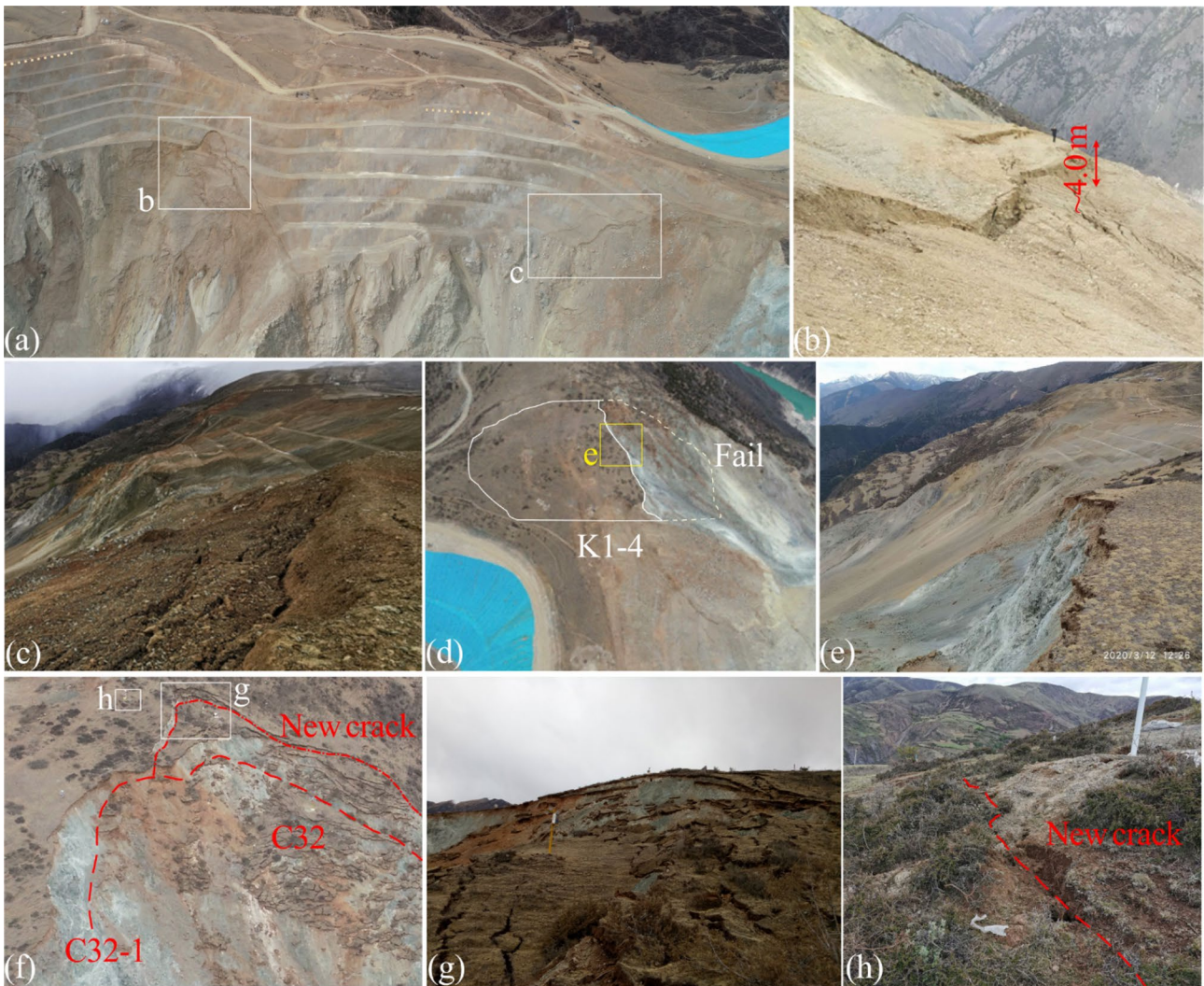
Fig. 15 Deformation-failure characteristics of K1: **a–c** deformation observed in the two spoil landfills at the front part of K1-1, **d** and **e** failure occurred in the front part of K1-4, **f** and **g** continuous expansion of deformation-failure range in K1-5, and **h** newly formed crack observed at the upper part of K1-5

failure surfaces for intensive deformation areas are determined on the basis of the combination of severe hole sticking and slurry leakage, as well as the features of the rock cores, which are reasonable according to the available data. However, the borehole cataloging results from Fig. 7 show that bedrock with fractured structure extends down to a depth greater than 100 m in this area. This suggests that there may be deeper or multiple failure surfaces at these areas. This can be explained as follows. (i) Many boreholes crossed the broken rock masses so that our borehole depths are generally between 50 and 70 m. As a result,

it is not possible to determine if any special fractured stratum exists below 70 m. (ii) The identified failure surfaces are mainly controlled by highly weathered serpentinite, carbonaceous slate, and brecciated rock, all of which easily serve as failure surfaces because of poor mechanical behavior. However, the evolution of a through-going failure surface by progressive development of shear surface stepping up and along non-persistent discontinuities for other fragment rocks (Eberhardt et al. 2004), such as the sericite phyllite in K2-1, is non-negligible in the long-term evolution process of a large-scale rockslide.
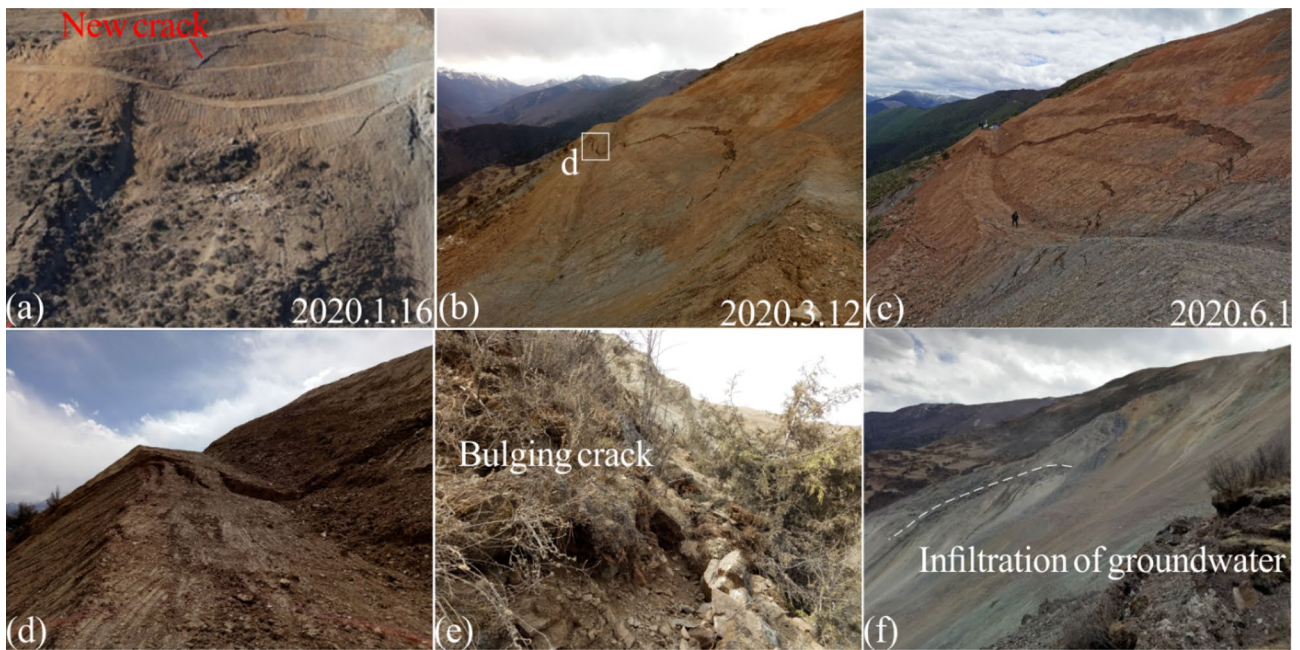
Fig. 16 Deformation-failure characteristics of K2: **a**–**d** a new arc-shaped crack and continuous propagation processes in K2-1, **e** a bulging crack observed at the front part of K2-1, and **f** a band of groundwater seepage in the front part of K2-1

Fig. 17 Deformation-failure characteristics of K3: **a** step-by-step gradual disintegration in K3-1 and **b** local collapse in the front part of K3-1
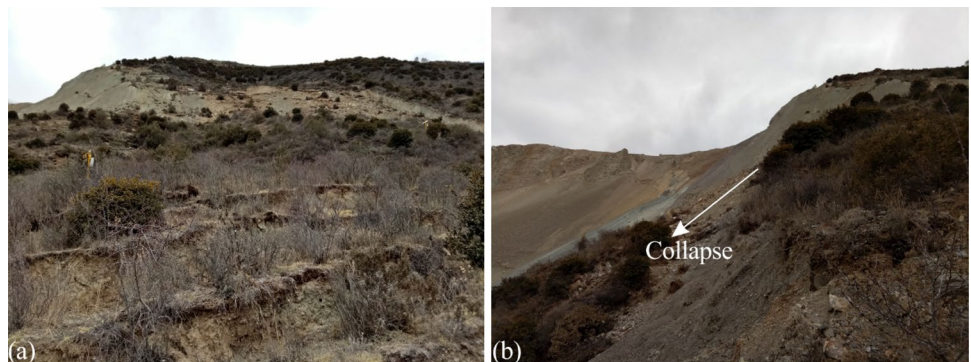

Fig. 18 Inferred failure surface for K2-1 and K3-1: **a** highly weathered carbonaceous slate at depth of 15 m in ZK 17 and **b** brecciated sandstone at depth of 19–21 m in ZK 18

Conclusion

A comprehensive multidisciplinary study involving field surveys and displacement measurements for analyzing the active features and geological evolution models of three unstable rockslide areas formed near the Baige landslide scar after two successive failures is presented in this paper. The main conclusions are as follows:

1. The rockslide areas are further subdivided into eleven subdomains, representing geo-structures that highlight the features of the geological structure belt accompanied by extremely active multiple-stage tectogenesis and characterized by varying metamorphism, deformation, and weathering. Several faults, fracture zones, and folds can be identified within the rockslide areas. The rock masses are characterized by widely distributed and variable interbedded lithologies with heterogeneous qualities combined with fragmentation, brecciation, and mylonitization.

2. The movements of rockslide areas are continuous and show a trend of gradual increase, especially encountering rainfall. The movement processes are ascribed to the dramatic unloading resulting from sudden large-scale detachments during the two successive landslides and progressive time-dependent strength degradation of the rock masses. However, the active features vary among different subdomains, which are intensely related to the daylighting geo-structures. In particular, (i) serpentinite predominates the subdomains K1-4 and K1-5, showing fragile fracturing once the accumulative strength deterioration reaches a certain degree; (ii) highly weathered carbonaceous slate controls K2-1 showing "back-pushing" of en masse slide; and (iii) the better integrity of exposed rock masses, such as granite porphyry, causes K1-3 to exhibit "fore-pulling" of retrogressive superficial collapse.

3. Our results provide some referential insights into the deformation-failure characteristics and initiation mechanisms of larger rockslides leading up to the catastrophic landslides in tectonic suture zones.

References

Böhme M, Bunkholt HSS, Oppikofer T, Dehls JF, Hermanns RL, Eriksen HØ, Laukens TR, Eiken T (2016) Using 2D InSAR, dGNSS and structural field data to understand the deformation mechanism of the unstable rock slope Gamanjunni 3, northern Norway, in: Landslides and Engineered Slopes, Experience, Theory and Practice, CRC Press 443–449

Brideau MA, Yan M, Stead D (2019) The role of tectonic damage and brittle rock fracture in the development of large rock slope failures. Geomorphology 10:30–49

Chen F, Gao YJ, Zhao SY, Deng JH, Li ZL, Ba RJ, Yu ZQ, Yang ZK, Wang S (2021) Kinematic process and mechanism of the two slope failures at Baige Village in the upper reaches of the Jinsha River, China. Bull Eng Geol Env 80:3475–3493

Cao WT, Yan DP, Qiu L, Zhang YX, Qiu JW (2015) Structural style and metamorphic conditions of the Jinshajiang metamorphic belt: nature of the Paleo-Jinshajiang orogenic belt in the eastern Tibetan Plateau. J Asian Earth Sci 113:748–765

Eberhardt E, Stead D, Coggan JS (2004) Numerical analysis of initiation and progressive failure in natural rock slopes-the 1991 Randa rockslide. Int J Rock Mech Min Sci 41:69–87

Fan XM, Xu Q, Alonso-Rodriguez A, Subramanian SS, Li WL, Zheng G, Dong XJ, Huang RQ (2019) Successive landsliding and damming of the Jinsha River in eastern Tibet, China: prime investigation, early warning, and emergency response. Landslides 16:1003–1020

Ganerød GV, Grøneng G, Rønning JS, Dalsegg E, Elvebakk H, Tønnesen JF, Kveldsvik V, Eiken T, Blikra LH, Braathen A (2008) Geological model of the Åknes rockslide, western Norway. Eng Geol 102:1–18

Li HB, Li XW, Li WZ, Zhang SL, Zhou JW (2019a) Quantitative assessment for the rockfall hazard in a post-earthquake high rock slope using terrestrial laser scanning. Eng Geol 248:1–13

Li HB, Qi SC, Chen H, Liao HM, Cui YF, Zhou JW (2019b) Mass movement and formation process analysis of the two sequential landslide dam events in Jinsha River, Southwest China. Landslides 16:2247–2258

Martins-Campina B, Huneau F, Fabre R (2008) The Eaux-Bonnes landslide (Western Pyrenees, France): overview of possible triggering factors with emphasis on the role of groundwater. Eng Geol 55:397–404

Ouyang CJ, An HC, Zhou S, Wang ZW, Su PC, Wang DP, Cheng DX, She JX (2019) Insights from the failure and dynamic characteristics of two sequential landslides at Baige village along the Jinsha River, China. Landslides 16:1397–1414

Rose ND, Hungr O (2007) Forecasting potential rock slope failure in open pit mines using the inverse-velocity method. Int J Rock Mech Min Sci 44:308–320

Sichuan Huadi Construction Engineering Co., Ltd (SHCEC) (2013) Investigation on geological disasters after the "8.12" earthquake in Jiangda County, Tibet. Technical report, Chengdu. (In Chinese)

Stead D, Wolter A (2015) A critical review of rock slope failure mechanisms: the importance of structural geology. J Struct Geol 74:1–23

Wang WP, Yin YP, Yang LW, Zhang N, Wei YJ (2020) Investigation and dynamic analysis of the catastrophic rockslide avalanche at Xinmo, Maoxian, after the Wenchuan Ms 8.0 earthquake. Bull Eng Geol Env 79:495–512

Willenberg H, Evans KF, Eberhardt E, Spillmann T, Loew S (2008a) Internal structure and deformation of an unstable crystalline rock mass above Randa (Switzerland): part II-three-dimensional deformation patterns. Eng Geol 101:1–14

Willenberg H, Loew S, Eberhardt E, Evans KF, Spillmann T, Heincke B, Maurer H, Green AG (2008b) Internal structure and deformation of an unstable crystalline rock mass above Randa (Switzerland): part I-internal structure from integrated geological and geophysical investigations. Eng Geol 101:1–14

Wang XF, Ian M, Jian P, He LQ, Wang CS (2000) The Jinshajiang suture zone: tectono-stratigraphic subdivision and revision of age. Sci China, Ser D Earth Sci 43:10–22

Xiong ZQ, Feng GC, Feng ZX, Lu M, Wang YD, Yang DJ, Luo SR (2020) Pre- and post-failure spatial-temporal deformation pattern of the Baige landslide retrieved from multiple radar and optical satellite images. Eng Geol 55:397–404

Zhang LM, Xiao T, He J, Chen C (2019) Erosion-based analysis of breaching of Baige landslide dams on the Jinsha River, China, in 2018. Landslides 16:1965–1979

Zhang M, McSaveney M, Shao H, Zhang CY (2018a) The 2009 Jiweishan rock avalanche, Wulong, China: precursor conditions and factors leading to failure. Eng Geol 233:225–230

Zhang SL, Yin YP, Hu XW, Wang WP, Zhang N, Zhu SN, Wang LQ (2020a) Dynamics and emplacement mechanisms of the successive Baige landslides on the Upper Reaches of the Jinsha River, China. Eng Geol 278:1–13

Zhang SL, Yin YP, Hu XW, Wang WP, Zhu SN, Zhang N, Cao SH (2020b) Initiation mechanism of the Baige landslide in the upper reaches of the Jinsha River, China. Landslides 17:2865–2877

Shi-lin Zhang · Xie-wen Hu · Gang Luo
Department of Geological Engineering, Southwest Jiaotong University, Chengdu 610031, China

Yue-ping Yin(✉) · Wen-pei Wang · Sai-nan Zhu
Institute of Geo-Environment Monitoring, Geological Survey, Beijing 10081, China
Email: cug22017@163.com wangwp@cigem.cn

Zong-liang Li
Center of China Geological Survey, Chengdu 610081, China

Xin-ming Wu
No.915 Geological Team, Sichuan Bureau of Geology and Mineral Resources, Meishan 620020, China